

1 **Demands of visual processing hierarchy shape laminar compartmentalization of**
2 **attention modulation of luminance contrast in area V4**

3 Xiang Wang¹, Anirvan S. Nandy^{1,3†} and Monika P. Jadi^{1,2,3,*†}

4 ¹Interdepartmental Neuroscience Program, Yale University, New Haven, CT 06511

5 ²Department of Psychiatry, Yale University, New Haven, CT 06511

6 ³Department of Neuroscience, Yale University, New Haven, CT 06511

7 †senior author

8 *corresponding author (monika.jadi@yale.edu)

9

10 **ABSTRACT**

11 Contrast is a key feature of the visual scene that aids object recognition. Attention has
12 been shown to selectively enhance the responses to low contrast stimuli in visual area
13 V4, a critical hub that sends projections both up and down the visual hierarchy. Veridical
14 encoding of contrast information is a key computation in early visual areas, while later
15 stages encode higher level features that benefit from improved sensitivity to low contrast.
16 How area V4 meets these distinct information processing demands in the attentive state
17 is not known. We found that attentional modulation of contrast responses in area V4 is
18 cortical layer and cell-class specific. Putative excitatory neurons in the superficial output
19 layers that project to higher areas show enhanced boosting of low contrast information.
20 On the other hand, putative excitatory neurons of deep output layers that project to early
21 visual areas exhibit contrast-independent scaling. Computational modeling revealed that
22 such layer-wise differences may result from variations in spatial integration extent of
23 inhibitory neurons. These findings reveal that the nature of interactions between attention
24 and contrast in V4 is highly compartmentalized, in alignment with the demands of the
25 visual processing hierarchy.

26

27

28

29

30 INTRODUCTION

31 Voluntary attention is essential for sensory guided behavior and memory formation
32 (Petersen and Posner, 2012). Failures in sensory processing and selective attention are
33 aspects of many mental illnesses, including schizophrenia and mood disorders
34 (Fioravanti et al., 2005; McIntyre et al., 2010; Neuchterlein et al., 1991). Visual spatial
35 attention plays a critical role in visual sensory processing: It allows improved perception
36 of behaviorally relevant target stimuli among competing distractors by boosting the
37 apparent visibility of the target (Carrasco et al., 2004). At the neuronal level, attention
38 modulates the activity of cortical neurons that encode an attended visual stimulus at
39 various stages of visual processing (Bisley and Goldberg, 2003; Ghose and Maunsell,
40 2008; Moran and Desimone, 1985; Motter, 1993; Reynolds et al., 1999; Treue and
41 Martinez Trujillo, 1999; Treue and Maunsell, 1996). In visual areas such as V4 and MT,
42 attention modulates neuronal mean firing rates, increases their firing reliability, and
43 reduces the co-variability among pairs of neurons (Cohen and Maunsell, 2009; Mitchell
44 et al., 2007, 2009; Reynolds and Chelazzi, 2004; Treue and Martinez Trujillo, 1999).
45 However, the computational principles that underlie the activity of neuronal populations
46 that represent both sensory information and the attentional state remain poorly
47 understood (Moore and Zirnsak, 2017; Reynolds and Chelazzi, 2004).

48
49 Object recognition is mediated by a hierarchy of cortical visual processing areas that form
50 the ventral visual stream. Contrast is a key feature of the visual scene that aids object
51 recognition, and the encoding of contrast information is one of the most important
52 computations performed by early visual areas. On the other hand, visual features
53 represented in higher areas such as the inferotemporal (IT) cortex benefit from improved
54 sensitivity to low contrast stimuli (Avidan et al., 2002; Rolls and Baylis, 1986). Visual area
55 V4 is a critical hub in the ventral stream that sends feedforward projections to areas such
56 as IT and feedback projections to early visual processing areas (Anderson and Martin,
57 2006; Douglas and Martin, 1991; Van Essen and Maunsell, 1983). Attention has been
58 shown to selectively enhance the responses to low contrast stimuli (Martinez-Trujillo and
59 Treue, 2002; Reynolds et al., 2000). Attention mediated selective enhancement of low

60 contrast features is thought to aid invariant representations in higher object recognition
61 areas downstream of V4 (Roe et al., 2012). However, such a bias in the attention-
62 modulated feedback from V4 to upstream visual areas can disrupt the contrast-based
63 feature extraction functions of these stages. How area V4 meets these distinct information
64 processing demands of the visual processing hierarchy is not known. While attention can
65 enhance V4 responses in a contrast-independent manner (response gain) under certain
66 experimental conditions (Williford and Maunsell, 2006), an understanding of robust
67 mechanisms of feedback from V4 that does not interfere with the contrast landscape of
68 scene representations in early visual areas remains elusive.

69
70 One possibility is that distinct subpopulations in V4 mediate these functional demands.
71 Indeed, the sensory cortical sheet, including area V4, is not a homogeneous piece of
72 tissue along its depth; rather, it has a six-layered or laminar structure made up of multiple
73 cell classes, of both excitatory and local inhibitory kind, with largely stereotypical
74 anatomical connectivity between and within layers (Douglas and Martin, 2004). Layer 4
75 (the *input* layer) is the primary target of projections carrying visual information from early
76 areas, such as V1, V2, and V3 (Felleman and Van Essen, 1991; Ungerleider et al., 2008).
77 Visual information is then processed by local neural subpopulations as it is sent to layers
78 2/3 (the *superficial* layer) and layers 5/6 (the *deep* layer), which serve as output nodes in
79 the laminar circuit (Hirsch and Martinez, 2006; Rockland and Pandya, 1979). The
80 superficial layers feed information forward to downstream visual areas, such as IT (Borra
81 et al., 2010; Distler et al., 1993), whereas the deep layers send feedback information to
82 upstream early visual areas (Callaway, 1998; Gattass et al., 2014; Mehta et al., 2000;
83 Ungerleider et al., 2008). This anatomical organization suggests distinct functional roles
84 (D'Souza and Burkhalter, 2017), and differential attentional modulation of sensory
85 representation among cell-class and layers-specific neural subpopulations. In support of
86 this idea, a recent study of simultaneous depth recordings in visual area V4 has shown
87 layer-specific attentional modulation of average neuronal responses, reliability of
88 responses, and correlations between responses of pairs of neurons (Nandy et al., 2017).
89 Therefore, to fully understand the attentional modulation of sensory computations, it is

90 essential to investigate the modulation of sensory representation in these subpopulations.
91 Our broad hypothesis is that the attentional modulation of contrast computations in area
92 V4 is not homogeneous, but rather is layer- and cell-class specific and that these
93 differences reflect the different computational demands on these subpopulations.
94 Considering their key contribution to feedback projections to early visual areas, we
95 specifically expect that projection neurons in the deep layers show uniform attentional
96 modulation across all contrasts in order to minimally impact the faithful representation of
97 contrast landscape in their target areas.

98

99 In this study, we characterized layer- and cell-class specific neural subpopulations from
100 extracellular simultaneous laminar recordings of single neurons within area V4 of
101 macaque monkeys performing an attention-demanding task. Using unsupervised
102 clustering techniques on spiking properties, we distinguished five functional clusters of
103 neurons. We distinguished layer identities – superficial, input or deep – of these neurons
104 using features of local field potentials. To test our hypothesis, we characterized the
105 attentional modulation of contrast response functions in these sub-populations. We
106 interpreted our findings within a computational framework of attentional modulation of
107 contrast responses (Reynolds and Heeger, 2009), which yielded predictions for distinct
108 mechanistic roles of these neural subpopulations in attentive perception.

109

110 **RESULTS**

111 In the primate visual system, cortical sensitivity to features such as luminance contrast
112 varies with the locus of spatial attention; contrast response functions (CRF) of cortical
113 neurons are measured to quantify this dependence (Kastner and Ungerleider, 2000;
114 Reynolds and Chelazzi, 2004; Reynolds et al., 2000). However, the laminar- and cell-
115 class specific dependence of CRF on the attentive state is not known. Using linear array
116 electrodes, we recorded neuronal activity from well-isolated single units, multi-unit
117 clusters, and local field potentials (LFPs) in visual area V4 of two rhesus macaques (right
118 hemisphere in monkey A, left hemisphere in monkey C) during an attention demanding
119 orientation change detection task (Figure 1A, B; see Methods). We used current source

120 density (CSD) analysis to identify different laminar compartments (*superficial*, *input*, and
121 *deep*), and assigned isolated single units to one of the three layers (see Methods). In the
122 main experiment, we presented a sequence of paired Gabor stimuli with different
123 contrasts (Figure 1B); one stimulus was presented inside the receptive fields (RFs) of the
124 recorded neurons and the other at an equally eccentric location across the vertical
125 meridian. Attention was cued either to the stimuli within the neurons' RFs ("attend-in") or
126 to the stimuli in the contralateral visual hemifield ("attend-away").

127

128 **Attentional Modulation of Contrast Response Function**

129 To examine the effects of attention on individual neurons, we used the method of ordinary
130 least squares to fit each neuron's contrast responses from both attentional states to a
131 hyperbolic ratio function (Figure 1C). This function is described by four parameters: r_{max} ,
132 c_{50} , m , and n , where r_{max} is the attainable maximum response, c_{50} is the contrast at
133 which neuronal response is half-maximal, m is the baseline activity, and n describes the
134 nonlinearity of the function. Attention effects differ considerably for individual neurons.
135 Attention either enhances or suppresses neuronal responses at different contrast levels
136 (Figure 1D). We quantified the effect of attention on every recorded neuron by computing
137 the attentional modulation index (AMI) using contrast responses from both attention
138 conditions (see Methods). We saw a significant variance of AMI values at each contrast
139 level (Figure 1E). We also examined how attention impacts the values of best-fitting
140 parameters (Figure 1F). The mean AMIs for r_{max} and m are significantly higher than zero
141 (Mann-Whitney U test, $p < 0.01$ for both distributions), which is consistent with previous
142 observations in V4 (Williford and Maunsell, 2006). The same percentage change in r_{max}
143 and m (15% increase) supports an effect of contrast independent scaling by attention.
144 The average modulations of c_{50} and n are significantly smaller than zero (Mann-Whitney
145 U test, $p < 0.01$ for c_{50} and $p \ll 0.01$ for n), suggesting an increased sensitivity to low
146 contrast stimuli and a reduction in the sensitivity to contrast change, respectively. The
147 bootstrap sampling distributions of the mean difference from 0 support the average
148 attention effects on r_{max} , n and m (Figure 1G). These results indicate that the overall
149 effect of attention on V4 neuron responses cannot be simply explained as selective

150 boosting of low contrast. It is a combination of modulations in multiple parameters of the
151 contrast response function (Figure 1F, G).

152

153 **Classification of Single Units Using Electrophysiological Features**

154 To investigate whether attention modulates different classes of neurons uniformly or
155 differentially, we characterized classes of single units based on two electrophysiological
156 properties extracted from extracellular recordings: the peak-to-trough duration (PTD) and
157 the local variation (Lv). Properties of the action potential waveform, especially the PTD,
158 have been extensively used to classify neurons into narrow- (putative inhibitory) and
159 broad-spiking (putative excitatory) cells (Constantinidis and Goldman-Rakic, 2002;
160 Diester and Nieder, 2008; Hussar and Pasternak, 2009; Johnston et al., 2009; Kaufman
161 et al., 2010; Mitchell et al., 2007; Wilson et al., 1994). The shapes of average spiking
162 waveform for all single units in our data were also highly variable (Figure 2A). We
163 exploited the information structure in the entire waveforms by applying principal
164 component analysis (PCA). The correlation pattern between the first two components of
165 the PCA (cumulative percentages of explained variance: 59.62%, 83.10%) supported the
166 idea that neurons can be separated into meaningful clusters by waveform shape
167 measures (Figure 2B). The clusters generated by neurons' PTDs in the PCA component
168 space were minimally overlapped (Supp. Figure 2E). Therefore, we chose PTD instead
169 of PCA components as one of the classification features for further analysis since the
170 PTD is more interpretable.

171

172 Firing variability measures have been previously used as an additional electrophysiology-
173 based dimension along which neurons have been found to be separable (Anderson et al.,
174 2011; Ardid et al., 2015; Degenetais et al., 2002). We used Lv , a measure that effectively
175 characterizes neurons' intrinsic spiking, and controls the effect of transient variations in
176 firing rates (Shinomoto et al., 2003) (see Methods). To achieve stable classification of
177 single units across attention conditions, we verified that Lv was not significantly
178 modulated by attentional states (Figure 2C).

179

180 We used a meta-clustering analysis based on the *k*-means clustering algorithm (see
181 Methods) in the two-dimensional space of PTD and *Lv*, and identified five clusters of
182 isolated single units (Figure 2D) (Ardid et al., 2015; Hartigan and Wong, 1979). The five-
183 cluster result was picked because it was the largest set of distinct cell classes that
184 characterized a majority (99.7%) of single units in the dataset (Supp. Figure 2A). Narrow-
185 spiking cells become a cluster by themselves, while those classified as broad-spiking cells
186 (Mitchell et al., 2007; Nandy et al., 2017) are split into four clusters. Based on the average
187 PTD and *Lv* of each cluster, we termed these five clusters as Narrow, Medium Regular,
188 Medium Bursty, Broad Regular, and Broad Bursty.

189
190 We validated our classification results using several methods (see Methods). First, we
191 gathered additional support for the meta-clustering based number of clusters by applying
192 a data-driven approach based on a novel form of cross-validation (Fu and Perry, 2020).
193 The method incorporates clustering results from the unsupervised algorithm into its
194 supervised training of linear classifiers to produce cross-validation errors (see Methods).
195 The five-cluster result showed the lowest cross-validation error (Supp. Figure 2B).
196 Second, we validated the stability of the clustering result by bootstrap subsampling
197 analysis (Hennig, 2007). The Jaccard similarity, averaged across subsamples, is a
198 measure of each cluster's robustness regarding its sensitivity to the amount of data. All
199 clusters in the five-cluster result had average Jaccard similarities greater than 0.5,
200 implying that clusters remained stable under subsampling (Supp. Figure 2C). A cell-wise
201 co-clustering matrix showing the probability that each pair of neurons belongs to a same
202 cluster across all subsamples also supported the number of clusters we chose (Supp.
203 Figure 2D). Third, we visualized our dataset by applying nonlinear transformations: t-SNE
204 (Hinton and Roweis, 2003) and UMAP (McInnes et al., 2018). Although these techniques
205 are generally suited for embedding high-dimensional data for visualization in a low-
206 dimensional space, their algorithms that enlarge the distance differences in the original
207 dataset also make them useful for recovering well-separated clusters. When we explored
208 the hyperparameters of both algorithms, we found that most of the five clusters were still
209 separable in both t-SNE and UMAP space (Figure 2E; Supp. Figure 2G, H). Notably, all

210 four non-Narrow clusters were separable, including the Medium Regular and the Medium
211 Bursty which occupied distinct locations in the t-SNE and UMAP space (Supp. Figure 2G,
212 H).

213
214 One of the assumptions we made to use the PTD as a clustering feature was that it
215 captures a significant amount of the variations of neurons' spiking waveforms. We tested
216 this assumption by clustering neurons in the principal component space of the AP
217 waveform and comparing them with neuronal groups defined by their PTD. We divided
218 neurons into narrow- (0-250 μ s), medium- (250-350 μ s), and broad-spiking (350-550 μ s)
219 groups, and found that the 3 clusters generated from the *k*-means clustering were
220 consistent with the 3 neuronal groups defined by the spike width (Supp. Figure 2F).

221
222 The clusters differ in terms of their firing rates (Supp. Figure 2I). Notably, Narrow class
223 neurons exhibited higher firing rates than the Broad Regular cluster when averaged
224 across layers (mean 10.2 Hz compared to 5.6 Hz, Mann-Whitney U test, $p < 0.05$). It is in
225 agreement with previous findings that narrow-spiking neurons, considered putative
226 inhibitory interneurons, show higher firing rates than broad-spiking neurons, thought to
227 be putative excitatory pyramidal cells (Connors and Gutnick, 1990; McCormick et al.,
228 1985; Mitchell et al., 2007; Nowak et al., 2003; Povysheva et al., 2006).

229

230 **Cell-Class and Layer-Specific Attentional Modulation**

231 We next examined how attention modulates contrast responses for each cell class. We
232 first computed the AMIs of best-fitting CRF parameters for every cell class. The pattern
233 of modulations of CRF parameters was distinct for individual cell classes (Figure 2F).
234 Narrow and Medium Regular cell classes showed significant positive modulations of
235 r_{max} only, implying a contrast-independent effect by attention. On the other hand, both
236 Broad Regular and Broad Bursty classes showed significant negative modulations of c_{50}
237 (Figure 2F), suggesting a selective enhancement of responses to low contrast stimuli.
238 This effect was novel to these classes and not revealed in the analysis of unclassified
239 neurons (Figure 1G). None of the remaining cell classes – Narrow, Medium Bursty and

240 Medium Regular – showed a significant modulation of c_{50} by attention, an effect that
241 matched the analysis of unclassified neurons (Figure 1G). Medium Bursty neurons
242 showed a modulation pattern that was distinct from the ones for any of the other four cell
243 classes: significant positive modulations of r_{max} and baseline activity, implying a pure
244 response gain effect by attention.

245

246 To further investigate the cell-class specific attentional modulation at each contrast level,
247 we computed the AMI as a function of contrast using CRFs from both attentional states
248 for every single unit and then averaged AMIs across single units within a cluster (Figure
249 3A, left panel). We found that the AMIs of Narrow and Medium Regular classes were
250 relatively less dependent on contrast, whereas the remaining clusters appeared to be
251 modulated by attention in a contrast-dependent manner (Figure 3A, left panel). When
252 averaged across all contrasts, attention positively modulated firing rates for all cell classes
253 except the Medium Regular class (Mann-Whitney U test, $p < 0.01$ except for MR). Further,
254 attentional modulation differed in significant ways among the non-Narrow clusters (Figure
255 3A, right panel). To quantify the contrast dependence of attentional modulation for each
256 single unit, we first averaged the AMIs within the low-contrast and the high-contrast
257 ranges with the contrast boundary set at each unit's best-fitting c_{50} parameter. We then
258 defined the contrast dependence index (CDI) of a single unit as the difference between
259 the two average AMIs normalized by the AMI averaged across all contrasts (see Methods).
260 Contrast independent modulation would then result in $CDI = 0$, reflecting a pure scaling
261 effect of attention on the CRF. A positive CDI would indicate a more robust attentional
262 modulation at the low-contrast range. A negative CDI would suggest a stronger attention
263 effect on neural responses at the high-contrast range (Figure 3B). We examined the CDI
264 distribution within each cell class and found that the Narrow and Medium Regular classes
265 showed small mean CDIs, and their distributions were not significantly different from zero.
266 However, the other 3 clusters (Medium Bursty, Broad Regular, Broad Bursty) exhibited
267 more positive CDIs (Figure 3C). These results are consistent with our findings of AMIs of
268 CRF parameters for each cell class (Figure 2F), confirming that attention modulated
269 Narrow and Medium Regular cell classes' responses regardless of the stimulus contrast.

270 On the other hand, the modulations for Medium Bursty, Broad Regular, and Broad Bursty
271 classes were dependent on contrast and were more robust in the low-contrast range.

272

273 We further inspected the laminar profile of the attention effect and its contrast
274 dependence for every cell class (Figure 3D, E). We excluded from our analysis clusters
275 that contained an insufficient number of units ($n < 10$) in a layer. When averaged across
276 contrasts, (Figure 3D, right panels), Narrow class neurons showed significant attentional
277 modulations in the input layer, but not in the superficial or deep layer (Figure 3D, right
278 panels, Mann-Whitney U test, $p_{\text{superficial}} = 0.79$, $p_{\text{input}} < 0.01$, $p_{\text{deep}} = 0.06$). On the other
279 hand, Broad Regular neurons were robustly modulated by attention across all cortical
280 layers (Figure 3D, right panels, Mann-Whitney U test, $p_{\text{superficial}} \ll 0.01$, $p_{\text{input}} \ll 0.01$, p_{deep}
281 $\ll 0.01$). The AMI difference between these two cell classes is in agreement with the
282 differences between narrow- and “broad”-spiking cells previously reported in these
283 cortical layer (Nandy et al., 2017); it is important to note that the AMI patterns across
284 layers were distinct for the other three cell classes (Figure 3D). Two key laminar patterns
285 of contrast dependence emerged from these 5 clusters. First, the attentional modulation
286 of the Narrow cell class was independent of contrast across all cortical layers. Second,
287 the Broad Regular cell class exhibited a strong contrast dependence and, specifically, a
288 significant modulation in the low-contrast range in the superficial and input layers; but its
289 dependence on contrast was not significant in the deep layer (Figure 3E). It is important
290 to note that at least one non-Narrow class (Medium Regular) was functionally similar to
291 Narrow neurons in superficial and input layers. Also notably, the laminar differences did
292 not emerge when all units in a layer were analyzed as either a single class or more
293 conventionally as narrow vs. “broad” classes.

294

295 **Laminar network mechanisms of contrast dependence of AMI across layers**

296 We next used computational modeling to gain insights into the possible neural
297 mechanisms underlying the layer- and cell-class specific AMI dependency on stimulus
298 contrast. Variation in CDI across experimental paradigms has been previously observed
299 (Martinez-Trujillo and Treue, 2002; Reynolds et al., 2000; Williford and Maunsell, 2006),

300 and explained by paradigm-specific normalization due to attention (Reynolds and Heeger,
301 2009). We hypothesized that normalization mechanisms can also explain the layer-
302 specific differences in CDI in our empirical findings (Figure 3D, E). To test this, we first
303 interpreted our results in the context of the normalization model of attention (Reynolds
304 and Heeger, 2009) to generate predictions about layer-specific cortical connectivity that
305 might underlie the variations in CDI. The normalization model of attention proposes a
306 computational principle that accounts for various attention effects on neurons' contrast
307 response functions (Reynolds and Heeger, 2009). Normalization model assumes that the
308 relative sizes of excitatory receptive field and suppressive field of neurons, and the
309 'attention field' of the experimental paradigm shape the net suppressive drive to individual
310 neurons. The suppressive drive ultimately determines the CDI of individual neurons in a
311 population. We thus investigated the consequences of varying the relative sizes of
312 excitatory receptive field and suppressive field of individual neurons on attentional
313 modulations of CRFs (see Methods). This inquiry was motivated by the observation that
314 neuronal receptive field sizes change along the cortical depth in sensory areas (Gilbert,
315 1977; Sur et al., 1985; Vaiceliunaite et al., 2013), and based on the assumption that
316 'attention field' sizes are constant for an experimental paradigm.

317

318 We simulated the normalization model with different sizes of excitatory receptive field and
319 suppressive field of neurons, and generated neuronal responses to different stimulus
320 contrasts in "attend in" and "attend away" conditions (Figure 4A, top panel). We computed
321 the AMI and the CDI for each combination of size parameters (see Methods). We find
322 that the CDI depends both on the excitatory receptive field size and on the suppressive
323 field size. Holding the attention field size and the stimulus size fixed, a smaller
324 suppressive field or a smaller excitatory receptive field leads to a greater CDI of the
325 attentional modulation (Figure 4A, middle panel). On the other hand, a larger suppressive
326 field or a larger excitatory receptive field results in a smaller CDI (Figure 4A, middle panel).
327 These results hold for a wide range of values of the stimulus size and the attention field
328 size. The pattern is robust when the attention field and the stimulus are both small or large
329 (Supp. Figure 4B, i). The results are also stable for both a linear and saturating transfer

330 function assumption between the stimulus contrast and excitatory drive in the
331 normalization model (Supp. Figure 4B, ii). We also computed the AMI of suppressive drive
332 of neurons for each combination of size parameters. The CDI of model neurons is roughly
333 proportional to the AMI of suppressive drive (Figure 4A, bottom panel). Greater the AMI
334 of suppressive drive, stronger is the CDI of model neurons, and vice versa. Since Broad
335 Regular neurons are putative excitatory pyramidal cells, these results suggest two
336 possible neural mechanisms that explain the laminar profile of CDIs of Broad Regular
337 neurons: the suppressive field size increases along the depth of V4 (Figure 4A, middle
338 panel) or the excitatory receptive field is more extensive in the deeper layer of V4 (Supp.
339 Figure 4C).

340

341 The normalization model predicts the AMI of the suppressive drive (Figure 4A, bottom
342 panel) to be correlated with the CDI of neuronal responses (Figure 4A, middle panel)
343 (Reynolds and Heeger, 2009). However, the suppressive field in the model can be
344 implemented by various biophysical mechanisms (Carandini, 2004). One possible
345 mechanism is shunting inhibition via lateral connections from other neurons in the cortical
346 neighborhood (Carandini and Heeger, 1994; Carandini et al., 1997; Kouh and Poggio,
347 2008), in which case the receptive field of local inhibitory neurons can approximate the
348 suppressive field. Since the average AMI of the putative inhibitory (Narrow) cluster and
349 CDI of putative excitatory (Broad) clusters in the input and deep layers in our empirical
350 data (Figure 3D right panels, Figure 3E) is also correlated, we further explored this
351 mechanism mediated by local inhibitory neurons. Under this assumption, the prediction
352 about the changes in suppressive field size down the cortical depth from the normalization
353 model transforms into one about changes in the excitatory (E) - inhibitory (I) connectivity
354 along the cortical depth. Similarly, the prediction about the changes in excitatory receptive
355 field sizes down the cortical depth can also transform into one about the changes in the
356 E-E connectivity along the cortical depth (Gilbert and Wiesel, 1985; Hirsch and Gilbert,
357 1991). The layer-specificity of cortical connectivity implies different temporal signatures
358 of neural activity across layers.

359

360 We next used a spiking network model to examine the effects of excitatory and inhibitory
361 receptive field sizes on spike-time correlation between populations of local excitatory (E)
362 and inhibitory neurons (I). Our spiking network model focuses on connectivity
363 mechanisms for generating variable sizes of suppressive and excitatory receptive fields
364 in a cortical network. The amplitude of the spike-time correlation between neurons has
365 been shown to depend on both the connection strength and the background synaptic
366 noise (Ostojic et al., 2009). Therefore, the spike-time correlation between neurons can be
367 a proxy for the size of the postsynaptic neuron's receptive field. We hypothesized that a
368 smaller receptive field of the postsynaptic neuron would make the local connections more
369 dominant against background inputs and lead to a higher spike-time correlation between
370 the locally connected neurons. We examined how spike-time correlations change as a
371 function of the inhibitory or excitatory receptive field size in a conductance-based model
372 of spiking neurons (see Methods). We set up 10 local networks or "columns" of E and I
373 units that were interconnected in a ring formation (Figure 4B, Supp. Figure 4C). Neurons
374 within the same column were mutually coupled, while interactions between columns were
375 confined to excitatory connections to local E and I neurons whose strengths decayed with
376 distance between columns. All connections occurred with a probability of 0.5. We
377 modeled the receptive field size as the standard deviation (σ_I or σ_E) of the connection
378 strength between columns (Figure 4B, Supp. Figure 4C). We performed simulations that
379 generated spiking activity in response to a step input (Figure 4B, bottom panel). The
380 spike-time correlation between local E and I populations was calculated using pooled
381 spike trains within the same column; the resulting spike-time correlation was averaged
382 across columns. We found that the inhibitory receptive field size has a critical impact on
383 the spike-time correlation amplitude in such a network (Figure 4C), while the excitatory
384 receptive field size has little effect (Supp. Figure 4C). A larger inhibitory receptive field
385 (larger values of σ_I) leads to a lower spike-time correlation between the local E and I
386 populations in the network (Figure 4C). This result suggests that the prediction about
387 inhibitory receptive field sizes down the cortical depth as the basis of CDI variation of
388 Broad Regular neurons can be tested by examining the spike-time correlation between
389 local E and I populations within each layer.

390

391 To test this prediction in our dataset, we computed the session-averaged spike-time
392 correlation between Narrow (putative inhibitory neurons) and Broad Regular (putative
393 excitatory neurons) single units within each layer (see Methods). We found that the spike-
394 time correlation amplitudes were higher in the superficial layer and the input layer than
395 that in the deep layer (Figure 4D). We compared the spike-time correlations in the deep
396 layer with those in either superficial or input layers, averaged within 3 different 50ms time
397 windows. The 95% confidence interval of the mean difference between layers in either
398 comparison was greater than 0 for the center window (Supp. Figure 4D). In accordance
399 with our findings from the E-I network models (Figure 4C), this suggests that inhibitory
400 neurons in the deep layer exhibit relatively broader receptive fields, which supports the
401 prediction by the normalization model of attention (Figure 4A, middle panel). Our findings
402 thus provide a parsimonious explanation for the layer- and cell-class specific contrast
403 dependence of attentional modulation observed in area V4 (Figure 4E).

404

405 **DISCUSSION**

406 Spatial attention plays a critical role in sensory guided behavior. It is thought to achieve
407 this by enhancing the responses to low contrast stimuli in mid-tier visual cortical areas
408 such as V4. While later stages of the visual processing hierarchy are thought to benefit
409 from this manipulation, V4 also sends feedback projections to early visual areas that use
410 veridical representation of contrast to aid object recognition. How area V4 meets these
411 distinct information processing demands is not known. Contrary to the simplifying
412 assumptions of prior empirical studies, we tested the hypothesis that V4 customizes its
413 output to different stages of the visual processing hierarchy through layer- and cell-class
414 specific attentional modulation of contrast computations. Recent advances in
415 experimental techniques have shown layer- and cell-class specific functional specificity
416 of computations in the cortical circuit (Adesnik and Naka, 2018; Adesnik and Scanziani,
417 2010; Naka and Adesnik, 2016; Olsen et al., 2012). However, these studies have been
418 limited to species in which higher cognitive functions, such as attention, are challenging
419 to study. Using computational approaches on laminar neural data in area V4 of the

420 macaque, we find that the attentional modulation of neural responses to visual luminance
421 contrast is indeed layer- and cell-class specific. We classified neurons into five functional
422 cell classes defined by their action potential widths and the statistics of firing variability
423 (Figure 2D); these classes show specificity in attention effects on their contrast response
424 functions (Figure 2F) and the contrast dependence of attentional modulation (Figure 3C).
425 Specifically, Narrow neurons show contrast-independent response modulation across
426 layers; Broad Regular neurons, the putative projection neurons, exhibit significant
427 contrast dependence of attentional modulation in the superficial layers, that project to
428 higher level visual areas, but not in the deep layers, that project to earlier visual areas
429 (Figure 3D, E). Notably, this highly significant laminar difference was not observable
430 without cell-class identification. These results provide the first evidence for our broad
431 hypothesis that attentional modulation of contrast computations in the visual cortex is
432 heterogeneous across those cell classes and layers that project to distinct stages of the
433 visual processing hierarchy. The qualitative nature of the attention modulation of contrast
434 in our data is not only distinct but suggests optimization for the computational demands
435 of the target stages. Selective boosting of responses to low contrast stimuli is
436 compartmentalized to the superficial output layers that project representations such as
437 extended contours and object surfaces to higher areas (see Roe et al., 2012 for a review).
438 Contrast-independent scaling of neural responses is confined to the deep output layers.
439 Neurons in these layers project back to early visual areas that are reliant on faithful
440 representation of luminance contrast for low-level feature extraction. We speculate that
441 the contrast-independent attentive feedback provides a spatial boost signal to early visual
442 areas that do not receive direct inputs from attention control centers such as the frontal
443 eye fields (Ungerleider et al., 2008). This also aligns with the predictive coding model of
444 object recognition, wherein V4 is a higher-level area in the object recognition hierarchy
445 that generates predictions of lower-level activity, without corrupting the sensory
446 landscape that is needed for error correction (Rao and Ballard, 1999).

447

448 When interpreted within the framework of the normalization model of attention (Figure
449 4A), the layer-specific attention modulation predicts differences in the spatial pooling of

450 local inhibitory populations across layers. Such differences further predict a layer-specific
451 signature of correlations between the activities of local inhibitory and putative excitatory
452 neurons when explored in a spiking E-I network model (Figure 4B, C). We find robust
453 evidence for differences in inhibitory spatial pooling across layers through our analyses
454 of correlations between putative inhibitory and putative excitatory neurons in the
455 superficial, input, and deep layers of the cortex (Figure 4D, E).

456

457 **Classification of cell-types**

458 The duration of the extracellular spike waveform has been used to distinguish putative
459 inhibitory interneurons from putative excitatory pyramidal cells in a wide range of species
460 and across various brain regions (Ardid et al., 2015; Bruno and Simons, 2002;
461 Constantinidis and Goldman-Rakic, 2002; Csicsvari et al., 1999; Fox and Ranck, 1981;
462 Frank et al., 2001; Mitchell et al., 2007; Nandy et al., 2017; Rao et al., 1999; Simons,
463 1978; Swadlow, 2003; Wilson et al., 1994). In terms of attention effects, narrow-spiking
464 neurons show stronger attention-dependent increases in absolute firing rates and firing
465 reliability than broad-spiking cells (Mitchell et al., 2007). Statistics of the firing pattern and
466 unsupervised clustering algorithms are also effective in identifying subpopulations of
467 neurons with distinct functional properties (Ardid et al., 2015; Compte et al., 2003;
468 Gouwens et al., 2019; Hawken et al., 2020; Shinomoto et al., 2009). It is important to note
469 that the clusters we distinguished based on spike width and firing variability may not
470 correspond to neuronal classes differentiated based on morphology or protein expression
471 patterns (Migliore and Shepherd, 2005; Tasic et al., 2018; Zeng and Sanes, 2017). Two
472 possible correspondences exist between the Narrow neurons and interneurons, and
473 between the Broad Regular neurons and pyramidal cells (Connors and Gutnick, 1990;
474 McCormick et al., 1985; Nowak et al., 2003). We find significant differences in both the
475 firing rate (Supp. Figure 2I) and the attentional modulation of firing rates (Figure 3A, D)
476 between clusters, suggesting their different functional roles in attention-mediated visual
477 processing. Crucially, these distinct functional roles are reflected by the differences in
478 contrast dependence of attentional modulation.

479

480 **Relation to prior studies of spatial attention in V4**

481 Prior studies evaluating attention effects on neuronal contrast responses proposed either
482 contrast-independent scaling of responses, termed as response gain (McAdams and
483 Maunsell, 1999a; Morrone et al., 2002; Pestilli et al., 2009; Treue and Martinez Trujillo,
484 1999) or boosting of responses to low contrast stimuli, termed as contrast gain (Li and
485 Basso, 2008; Li et al., 2008; Martinez-Trujillo and Treue, 2002; Reynolds et al., 2000) or
486 an intermediate effect between the two (Huang and Dobkins, 2005; Williford and Maunsell,
487 2006). Although the overall attentional modulation of best-fitting CRF parameters in our
488 dataset is consistent with the intermediate effect (Figure 1F, G), attention effects on
489 individual clusters are highly variable: a mixture effect of response gain and contrast gain
490 is observed for Broad Regular and Broad Bursty units; Medium Bursty cluster shows a
491 response gain change; Medium Regular and Narrow neurons are only modulated in their
492 maximum responses (Figure 2F). Furthermore, some clusters, such as Broad Regular
493 and Broad Bursty neurons, exhibit larger attention-dependent increases in response than
494 the population mean, especially within the low-contrast range (Figure 3A). These
495 observations suggest that attentional modulation of firing rate for certain cell classes may
496 be more robust than that gleaned from previous studies that averaged across the whole
497 recorded population. These cell-class specific increases in firing rate may significantly
498 improve the signal-to-noise ratios of individual cell classes, and therefore, act as another
499 important contributor to the improvement of psychophysical performance due to attention
500 in addition to reductions in correlations (Cohen and Maunsell, 2009; Mitchell et al., 2009).

501

502 **Our interpretation of the normalization model**

503 The predictions from the normalization model (NM) of attention provide one possible
504 explanation for the diverse contrast modulation patterns across layers. NM assumes both
505 stimulus parameters and attention condition to contribute to the normalization input to
506 local excitatory neurons. The stimuli presented in our experiments were optimized for the
507 recording site and did not change with attention condition, and hence are not assumed to
508 contribute differentially to the normalization mechanism. NM also assumes the sizes of
509 attention field of the population to contribute to the normalization input to individual

510 neurons. The attention field in NM describes the attention gain for each neuron in the
511 population and depends on the animal's attentional strategy employed during the
512 experiment (Herrmann et al., 2010). The neural substrate for the attention field is
513 unspecified in the NM, but we assumed the attention field to be constant across the
514 cortical depth since the data was collected using a fixed experimental paradigm. However,
515 given a lack of the biophysical mechanism underlying attentional modulation, our
516 understanding of the attention field may be subject to future revision. The extent of
517 excitatory receptive field, also termed as the stimulation field, in the NM can be mediated
518 by various cortical connectivity patterns. While we explored a lateral pooling mechanism
519 as the determinant of the receptive field extent of neurons, innervation specificity of
520 feedforward synaptic input could be an alternative mechanism (Bruno and Simons, 2002;
521 Hubel and Wiesel, 1962).

522

523 The variation in contrast dependence of attentional modulation observed across layers
524 and cell classes (Figure 3D, E) in our data is explained by the NM in a most parsimonious
525 way via the variability of the suppressive field size (Figure 4). However, the NM is agnostic
526 to the neural machinery dedicated to the formation of neuronal tunings or the
527 implementation of attentional modulation. To explore the implications of its field size
528 predictions on spike-time correlations in a biophysical model, we considered the model's
529 stimulation field as the receptive field of putative excitatory projection neurons in a column,
530 and its suppressive field as the receptive field of local inhibitory interneurons.

531

532 We implemented a spiking network model to relate the NM's predictions of variable
533 suppressive field sizes to variations in spike-time correlations in our data. It is important
534 to note that our model is not a spiking network implementation of the entirety of attention
535 computations described by the NM. The suppressive field in NM, which mediates divisive
536 normalization, is a computation that can be implemented through a variety of
537 mechanisms (see Reynolds and Heeger, 2009 for review). We chose one of the candidate
538 suppression mechanisms – pooling of lateral inputs by local inhibitory interneurons
539 (Carandini and Heeger, 1994; Carandini et al., 1997; Troyer et al., 1998). A feedforward

540 mechanism of variable suppressive fields would yield a very similar prediction for spike-
541 time correlations between local E and I populations. Our choice was guided by excellent
542 agreement between the NM model AMI predictions and modulation patterns of related
543 clusters in the input and deep layers. It is, however, important to note that in the superficial
544 layers, putative inhibitory neurons (Narrow cluster) lack significant attention modulation
545 in spite of robust boosting of responses to low contrast stimuli in putative excitatory
546 neurons (Broad clusters). This does not agree with the predictions of the normalization
547 model. There are three possible explanations for this observation: 1. Suppressive drive
548 to broad-spiking neurons in superficial layer is not provided by local inhibitory neurons
549 within that layer. 2. Superficial layer broad-spiking neurons inherit their contrast
550 dependent attention modulation from the input layer. 3. Suppressive drive to broad-
551 spiking neurons in the superficial layer is provided by non-PV local inhibitory neurons
552 within the layer. Since PV neurons are a majority of the local interneuron population which
553 itself occupies roughly 20% of the total neural population in the cortex, it is highly possible
554 that our recordings did not sample the other inhibitory neuronal types. Indeed, studies
555 from the mouse visual cortex suggest that SOM+ neurons play a key role in mediating
556 lateral inhibition to layer 2/3 pyramidal neurons (Adesnik et al, 2012). Further studies are
557 needed to distinguish the contributions of local vs feedforward computations to the
558 attention effects in superficial layers.

559

560 When testing the model's predictions in our dataset, we ascribed the stimulation field to
561 any of the non-Narrow clusters, including the Broad Regular cluster identified in our layer-
562 specific CDI analysis (Figure 3E). We ascribed the suppressive field to the receptive field
563 of the Narrow cluster (putative interneurons). While the experimental data for the Broad
564 Regular cluster robustly validates the model predictions (Figure 4D), the Broad Bursty
565 and Medium Regular classes show a comparable trend (Supp. Figure 4D). We could not
566 perform a robust analysis for the remaining non-Narrow cell classes in a subset of layers
567 due to a lack of sufficient experimental data (Figure 3E).

568

569 **Conclusion**

570 Attention increases the signal detection abilities of individual neurons. Whether the
571 attention mediated firing rate variability is unchanged (McAdams and Maunsell, 1999b)
572 or reduced (Mitchell et al., 2007), the response gain alone results in improved signal-to-
573 noise ratio of individual neurons, and enhances the discriminability of the attended signal
574 (McAdams and Maunsell, 1999b; Verghese, 2001). Attention mediated increases in
575 neural responses to low- and intermediate-contrast stimuli can extend the separation
576 between the neuron's stimulus-evoked responses and its spontaneous activity, thereby
577 improving the neuron's sensitivity to low-contrast stimuli. There has, however, been a
578 long-standing debate regarding the nature of interactions between attention and visual
579 scene contrast that mediate object recognition. Previous theoretical studies have sought
580 to resolve this based on the nature of differences in experimental paradigms (Reynolds
581 and Heeger, 2009). Our work has exploited advanced experimental techniques to bring
582 novel understanding of these interactions. Superficial cortical layers in area V4 that
583 project to higher object recognition stages exhibit enhancement of low contrast stimuli.
584 Deep layers that project to earlier visual areas exhibit contrast independent attentional
585 scaling of neuronal responses. By identifying the compartmentalization of attention
586 modulation among cortical layers, our study has uncovered a new dimension: the nature
587 of interactions between attention and contrast is aligned with the demands of the visual
588 processing hierarchy. A previous study has suggested that encoding of scene contrast
589 and spatial attention by distinct neural populations in area V1 could fulfill its visual
590 processing demands in the face of contrast dependent attentional feedback (Pooremaeili
591 et al., 2010). Our work has revealed an elegant mechanism of meeting these needs via
592 laminar compartmentalization of attention modulation in area V4 that contributes to this
593 feedback. Low-frequency synchrony between the thalamus and visual cortex has been
594 suggested to guide the higher-frequency synchronization of inter-area activity that is
595 critical to the communication of attention signals between brain areas (Saalmann et al.,
596 2012). A contrast-independent effect of attention in the deep layer of V4 may also drive
597 alpha rhythms of pulvino-cortical loops irrespective of stimulus conditions and maintain
598 the transmission of attentional priorities across the cortex. Future studies are needed to

599 test these and related hypotheses about the different functional roles of contrast-attention
600 interactions in different cortical layers.

601

602 **FIGURE CAPTIONS**

603

604 **Figure 1. Attentional modulation of Contrast Response Function**

605 (A) Orientation change detection task. While the monkey maintained fixation, two oriented
606 Gabor stimuli were flashed on and off at two locations: one within the RF overlap region of the
607 recorded V4 column and the other at a location of equal eccentricity across the vertical
608 meridian. The covert attention of the monkey was cued to one of the two locations. One of the
609 two stimuli changed its orientation at an unpredictable time. The monkey was rewarded for
610 making a saccade to the location of orientation change (95% probability of change at the cued
611 location; 5% probability at uncued location [foil trials]). If no change happened (catch trials), the
612 monkey was rewarded for maintaining fixation.

613 (B) An example trial showing the single-unit signals in the attend-in condition. The time axis is
614 referenced to the appearance of the fixation spot. Spikes (vertical ticks) in each channel come
615 from the single unit with the highest spike rate in this trial. The gray boxes depict stimulus
616 presentation epochs. In this particular trial, 8 sample stimuli with different contrasts were
617 presented, followed by a target stimulus flash with an orientation change that the monkey
618 responded to correctly. Two different waveforms were shown for two single units.

619 (C) The mathematical function we used to fit neuronal contrast response functions is shown on
620 the top. Schematics at the bottom show the effect of positive attentional modulation of each
621 parameter on the contrast response functions.

622 (D) The best-fitting contrast response functions of three example neurons in “attend in” and
623 “attend away” conditions. Mean \pm SEM. Insets show the attentional modulation indices
624 calculated as a function of contrast.

625 (E) The AMI as a function of contrast for each of the 255 visually responsive single units, with
626 the three example units in (C) highlighted.

627 (F) Attention effects on the best-fitting parameters of the contrast response function. Each
628 histogram plots the AMI distribution of a particular parameter across the population, with the
629 dashed line marking the 0 modulation and the arrow with a number depicting the median AMI

630 value. The median AMI is significantly different from zero for all 4 parameters (Mann-Whitney U
631 test, $p < 0.01$).

632 (G) The mean difference of AMI from 0 for the 4 parameters are shown in the Cumming
633 estimation plot. Mean differences are plotted as bootstrap sampling distributions. Each mean
634 difference is depicted as a dot. Each 95% confidence interval (CI) is indicated by the ends of the
635 vertical error bars. The faded color represents that the 95% CI include 0.

636

637 **Figure 2. Classification of Single Units Using Electrophysiological Features.**

638 (A) Mean waveforms for all 410 single units recorded. Waveforms were smoothed using spline
639 interpolation and their heights were normalized to help compare spike widths.

640 (B) Distribution of all single units in the space of the first two principal components (PCs) of the
641 waveforms. The non-Gaussian structure implies that spike shape is a viable feature for
642 classifying single units.

643 (C) Histogram of the local variation AMI for all units with available local variation ($n=341$). The
644 dashed line marks the 0 AMI value. The arrow depicts the median value of the distribution. The
645 average local variation of the population is not significantly modulated by attention (Mann-
646 Whitney U test, $p = 0.37$).

647 (D) k -means clustering of 341 single units based on PTD and spiking variability. Cell classes are
648 named after their spiking widths (narrow, medium, broad) and their spiking patterns (regular,
649 bursty). Single units within each range of spike width are highlighted in the component space on
650 the top. Unclassified units are displayed as black crosses in the feature space.

651 (E) t-SNE embedding of the same data in (D) in a 2-dimensional space. The number at the left
652 bottom corner of each panel represents the perplexity parameter of the t-SNE embedding.

653 (F) The Cumming estimation plot shows the bootstrap sampling distributions of AMIs of CRF
654 parameters for each cell class. Distributions with CIs including 0 are displayed in faded colors.
655 The CRF parameters were only available for visually responsive single units.

656

657 **Figure 3. Contrast Dependency of AMI is Cell-Class and Layer-Specific**

658 (A) The left panel shows the AMI of contrast responses as a function of contrast averaged
659 across visually responsive single units in each cluster. Mean \pm SEM. The black line indicates
660 the population mean. The right panel shows the mean AMI averaged across contrast for each
661 cluster. Asterisk indicates either the distribution is significantly different from zero or two
662 distributions are significantly different (Mann-Whitney U test, $p < 0.05$).

663 (B) To quantify the contrast dependence of attentional modulation, we averaged the AMI for a
664 single unit separately within the low-contrast range and the high-contrast range (using the c_{50} as
665 the low- to high-contrast threshold). We then defined the contrast dependence index (CDI) as
666 the difference between the average AMI within the low-contrast range and that within the high-
667 contrast range, normalized by the mean AMI across the whole contrast range. The schematic
668 shows the interpretation of different ranges of CDI in terms of the AMI.

669 (C) The Cumming estimation plot shows the raw data of CDIs (left) and the bootstrap sampling
670 distribution of the mean (right) for each cell class. The plus signs are the outliers within the axis
671 range, and the arrows depict the outliers outside the axis limit. The number of valid units for
672 each cell class is shown on the top of the swarm plot. Distributions for cell classes with CIs
673 inclusive of 0 are shown in faded colors.

674 (D) Layer-wise AMI (mean \pm SEM) of contrast responses for each cell class as a function of
675 contrast (left) or averaged across contrast (right). Asterisk indicates either the distribution is
676 significantly different from zero or two distributions are significantly different (Mann-Whitney U
677 test, $p < 0.05$). Cell classes that contain fewer than 10 units (including outliers) are excluded.

678 (E) Layer-wise CDI for five clusters of units, all units, and non-narrow units. The Cumming
679 estimation plot shows the bootstrap sampling distribution of the mean CDI. Distributions with CIs
680 inclusive of 0 are illustrated in faded colors. The number of units excluding outliers is shown on
681 the top of each plot. Distributions for cell classes with CIs inclusive of 0 are shown in faded
682 colors. For the raw data of the layer-wise CDIs, see Supp. Figure 3B.

683

684 **Figure 4. Computational Models Provide A Parsimonious Explanation for the Laminar** 685 **Profile of AMI Contrast Dependence**

686 (A) Predictions from the normalization model of attention with different suppressive field sizes or
687 different excitatory (E) receptive field sizes. The top panel shows contrast response functions for
688 a simulated neuron in the normalization model, when attending to a stimulus within the neuron's
689 receptive field (black curve) and when attending toward the opposite hemifield (gray curve). The
690 orange curve represents the AMI. The black dot shows the inflection point of "attend away"
691 responses that was used to delimit the low- and high-contrast ranges. The middle panel shows
692 CDIs for simulated neurons as a function of the E receptive field size and the suppressive field
693 size while holding the stimulus size and the attention field size fixed. The white rectangles depict
694 a potential mechanism that leads to the observed variation of CDIs across layers (change in
695 suppressive field size). The black asterisk corresponds to the model parameters used for the

696 simulation above. The bottom panel shows AMIs of suppressive drive as a function of the E
697 receptive field size and the suppressive field size. For both simulations, the attention field size is
698 30 and the stimulus size is 5. The normalization model predicts the AMI of the suppressive drive
699 to be correlated with the CDI of neuronal responses.

700 (B) Simulations of a conductance-based E-I network with columnized connections. Schematics
701 of the E-I networks corresponding to the possible mechanism in (A) are shown on top. 800 E
702 and 200 I units were evenly distributed in 10 columns around a ring. We interpret the
703 normalization model's suppressive field as the receptive field of inhibitory neurons in the E-I
704 network model. E and I units from the same column are mutually coupled. We modeled I
705 receptive field size as the standard deviations (σ_I) of E-I connections (W_{ie}) across columns
706 (middle panel, -5 and 5 are the same column). We changed the range of E-I connections across
707 columns (W_{ie} , shades of green) while keeping other connections the same (gray, including W_{ee} ,
708 W_{ii} , W_{ei}). At the bottom, the raster plot shows the spiking activity for all units organized by their
709 column IDs (blue, I; red, E) in response to a step input. The box depicts a 200 ms window used
710 for computing cross-correlations between E and I populations.

711 (C) Cross-correlograms between E and I populations in the same column with different I
712 receptive field sizes. Cross-correlations were calculated using the pooled spike trains of E units
713 and I units from the same column across 500 repeats of identical simulation and averaged
714 across 10 columns. A larger I receptive field reduces the cross-correlation between local E and I
715 populations. Mean \pm SEM.

716 (D) Cross-correlograms (mean \pm SEM) between Narrow and Broad Regular cell classes in the
717 superficial, input, and deep layer. Cross-correlations were calculated using the pooled spike
718 trains of Narrow class (putative inhibitory) neurons and Broad Regular class (putative excitatory)
719 neurons, and were averaged across sessions. The arrows mark 3 time intervals during which
720 we averaged the cross-correlations and compared the mean differences between the superficial
721 (or input) and the deep layers. Asterisk: The mean difference of cross-correlations in the center
722 interval (-75 ms to 75 ms) has a 95% CI above 0. For the estimation plot, see Supp. Figure 4B.

723 (E) Proposed E-I networks in V4 accounting for the layer-wise CDI variations. The empirical
724 data and the model simulations imply a larger inhibitory pooling size in the deep layer than
725 those in the superficial and input layer. The arrows depict the canonical information flow
726 pathways in a columnar circuit.

727

728 **Supp. Figure 2. Validations for the Single-unit Classification and the AMI of CRF**

729 **Parameters for Each Cell Class**

730 (A) Percentage of classified neurons in the total sample as a function of the number of clusters
731 (k) input to the k -means clustering algorithm. The 5-cluster result was able to identify the largest
732 set of distinct clusters while classifying most of the units.

733 (B) Cross-validation (CV) errors for different numbers of clusters. The 5-cluster result shows the
734 lowest CV error.

735 (C) The minimum Jaccard index across clusters for each k from the subsampling analysis. The
736 analysis was applied to neuronal data from either of the two attention conditions or to combined
737 data. Clusters that have Jaccard indices above 0.5 are considered as stable.

738 (D) The cell-wise co-clustering matrix showing the probability of single units belonging to the
739 same cluster in the subsampling analysis.

740 (E) In the principal component space of spike shape, we colored single units based on their
741 spike width range (open circles; narrow, medium, broad). The clusters generated from the peak-
742 to-trough duration were minimally overlapped.

743 (F) In the principal component space of spike shape, we colored single units either based on
744 their spike width range (open circles; narrow, medium, broad) or by running the k -means
745 clustering algorithm with the first 2 PCs (closed circles). The clusters generated from the k -
746 means clustering match the ones grouped by the peak-to-trough duration, suggesting that peak-
747 to-trough duration is an efficient measure to capture the variance in spike shapes.

748 (G and H) Embedding the data used for the k -means clustering in a 2-dimensional space using
749 t-SNE (G) or UMAP (H).

750 (I) Mean firing rate for visually responsive single units split by cell class or by layer. Neuronal
751 firing rates were calculated from stimulus flashes with the highest common contrast across two
752 monkey experiments in the "attend away" condition. The number of single units within each
753 cluster is shown. In each layer, we only analyzed clusters containing more than 10 single units.
754 Asterisk indicates either the distribution is significantly different from zero or two distributions are
755 significantly different (Mann-Whitney U test, $p < 0.05$). Mean \pm SEM.

756 (J) The Cumming estimation plot shows the raw data (left) of AMIs of best-fitting CRF
757 parameters and the bootstrap sampling distribution of each cell class's mean (right).

758

759 **Supp. Figure 3. Raw Data of AMIs and CDIs of AMI for Each cell class**

760 (A) The AMI of firing rate as a function of contrast for single units within each cell class.

761 (B) The raw data of cluster-wise CDIs of AMI within each layer. The plus signs are the outliers
762 within the axis range, and the arrows depict the outliers outside the axis limit. The number of
763 valid units for each cell class is shown on the top of the swarm plot.
764 (C) Layer-wise AMI (mean \pm SEM) for all units, Narrow unit, and non-narrow units as a function
765 of contrast (left) or averaged across contrast (right). Asterisk indicates either the distribution is
766 significantly different from zero or two distributions are significantly different (Mann-Whitney U
767 test, $p < 0.05$).

768

769 **Supp. Figure 4. Normalization Model of Attention and CCG Analyses Between Cell**
770 **Classes**

771 (A) The structure of the normalization model of attention. The left panel shows a pair of
772 orientated grating stimuli with identical contrasts, acting as input to the model. The central black
773 dot indicates the fixation point. The dashed red circle indicates the receptive field of the model
774 neuron centered on the grating stimulus. The stimulus drive shown in the middle panel is a
775 collection of neural activity driven by the stimuli. Neurons are arranged based on their receptive
776 field center (horizontal position) and orientation preference (vertical position). The values of the
777 stimulus drive are shown by brightness. The top panel shows the attention field as a function of
778 the receptive field center and the orientation preference. In this case, the attention is guided to
779 the right stimulus position and does not vary with orientation. Gray areas indicate values of 1,
780 and white areas indicate values greater than 1. The suppressive drive at the bottom is
781 calculated from the point-by-point product of the stimulus drive and the attention field and then
782 pooled over space and orientation according to the suppressive field size. The stimulus drive is
783 multiplied by the attention field and then divided by the suppressive field to generate the output
784 firing rates of model neurons (right panel).

785 (B) i, CDIs for simulated neurons in the normalization model with different stimulus sizes and
786 attention field sizes. In each panel, we vary the E receptive field size relative to the attention
787 field size (x-axis), and the suppressive field size relative to the E receptive field size (y-axis).
788 The pattern of CDI holds for a range of values of stimulus size and attention field size. ii, CDIs
789 for simulated neurons in the normalization model with different types of inputs. We changed the
790 stimulus drive input to the normalization model to have either a nonlinear or an attention-
791 modulated contrast response function. We tested both the response gain (10% increase in
792 overall response) and the contrast gain (1% of increase in detected contrast) effects. For these

793 simulations, the attention field size is 30 and the stimulus size is 5. The pattern of CDI holds for
794 different types of inputs.

795 (C) Changes in E receptive field size (white box) can also lead to the variation of CDIs across
796 layers (left panel). We tested this hypothesis in the E-I network by adjusting the standard
797 deviation of between-column E-E connections (W_{ee}) from narrow (green) to broad (orange) while
798 keeping other connections the same (gray, including W_{ee} , W_{ii} , W_{ie}) (middle panel). Cross-
799 correlograms between E and I populations in the same column suggest that different E
800 receptive field sizes have little impact on the spike-time correlations of local neural activity
801 across layers (right panel).

802 (D) Cross-correlograms (mean \pm SEM) between Narrow and 3 other cell classes in the
803 superficial, input, and deep layer. Cross-correlations were calculated using the pooled spike
804 trains of Narrow class and the other cell class (Board Bursty, Medium Regular, or Medium
805 Bursty) and were averaged across sessions.

806 (E) The Cumming estimation plot shows the mean difference for cell-class specific comparisons
807 of average cross-correlations between the superficial (*Super.*) and deep layers or between the
808 input and deep layers. We picked 3 time intervals to compute the average cross-correlations
809 (rows). The raw data of average cross-correlations is plotted on the left in each panel. Each
810 mean difference between layers is plotted on the right as a bootstrap sampling distribution.

811

812 **METHODS**

813 *Attention Task and Electrophysiological Recording:*

814 Well-isolated single units were recorded from area V4 of two rhesus macaques during an
815 attention-demanding orientation change detection task (Figure 1A). The task design and
816 the experimental procedures are described in detail in previous studies (Nandy et al.,
817 2019; Nandy et al., 2017). While the monkey maintained fixation, two oriented Gabor
818 stimuli were flashed on for 200 ms and off for variable intervals (randomly chosen
819 between 200 and 400 ms). The contrast of each stimulus was randomly chosen from a
820 uniform distribution of 6 contrasts ($c = [10\%, 18\%, 26\%, 34\%, 42\%, \text{and } 50\%]$). One of
821 the stimuli was located at the receptive field overlap region of the recorded neurons and
822 the other at an equally eccentric location across the vertical meridian. At the beginning of
823 a block of trials, the monkey was spatially cued to covertly attend to one of the two spatial

824 locations using instruction trials in which only one stimulus was presented. One of the two
825 stimuli changed in orientation at an unpredictable time (minimum 1s, maximum 5s, mean
826 3s). The monkey was rewarded for making a saccade to the location of orientation change.
827 95% of the orientation changes occur at the cued location, and 5% occur at the uncued
828 location (foil trials). We observed impaired performance and slower reaction times for the
829 foil trials, suggesting that the monkey was indeed using the spatial cue to perform the
830 task. The difficulty of the task was controlled by changing the degree of orientation change
831 (randomly chosen from the following: 1°, 2°, 3°, 4°, 6°, 8°, 10°, and 12°). If no change
832 occurred before 5 s, the monkey was rewarded for holding fixation (catch trial, 13% of
833 trials).

834 While the monkey was performing the attention task, we used artificial dura chambers to
835 facilitate the insertion of 16-channel linear array electrodes (“laminar probes”, Plexon,
836 Plexon V-probe) or single tungsten microelectrodes (FHC Inc) into cortical sites near the
837 center of the prelunate gyrus. Neuronal signals were recorded, filtered, and stored using
838 the Multichannel Acquisition Processor system (Plexon). Neuronal signals were classified
839 as either isolated single units or multiunit clusters by the Plexon Offline Sorter program.
840 For the data collected from linear array electrodes, we used current source density
841 analysis (Mitzdorf, 1985) to identify the superficial (Layers 1-3), input (Layer 4), and deep
842 (Layers 5 and 6) layers of the cortex based on the second derivative of the flash-triggered
843 LFPs (Bollimunta et al., 2008; Schroeder and Lakatos, 2009; Schroeder et al., 1998;
844 Nandy et al., 2019; Nandy et al., 2017). Cell bodies of single units with bi-phasic action
845 potential waveforms were assigned to the same layer in which the electrode channel was
846 situated during recordings. Units that had tri-phasic waveforms or other shapes were
847 excluded from analyses. Extracellular data were collected over 32 sessions (23 sessions
848 in monkey A, 9 in monkey C) using linear array electrodes and 42 sessions (24 sessions
849 in monkey A, 18 in monkey C) using single tungsten electrodes, yielding 410 single units
850 in total (337 units using linear array electrodes and 73 units using single tungsten
851 electrodes). Unit yield per session was considerably higher in monkey C than monkey A,
852 resulting in a roughly equal contribution of both monkeys toward the population data.

853

854 *Contrast Response Function (CRF):*

855 Neuronal responses were analyzed only for correctly performed trials, excluding
856 instruction trials. We restricted all data analysis to non-target stimuli because neuronal
857 responses to target stimuli were generally affected by the behavioral response or the
858 reward delivery, which occurs on correct trials after the target's appearance. Moreover,
859 the larger number of non-target stimuli compared to target stimuli provided a more reliable
860 response strength measure. For both attention conditions, the firing rate of a single unit
861 in response to a particular contrast was measured by counting the number of spikes within
862 a period of 60-260 ms after stimulus onset. Its baseline firing rate in each attention
863 condition was extracted from a 200 ms window before a stimulus flash. The mean firing
864 rates and the standard deviations (SDs) were generated across all stimulus flashes. We
865 considered a neuron as visually responsive if any contrast responses exceeded its
866 baseline firing rate by 4 SDs for both attention conditions. We found that 255 of 410 single
867 units were significantly driven by the task stimuli and had valid Lv measures (See
868 *Analysis of Spiking Activity*).

869 We drew 1000 random samples of contrast responses from a normal distribution with the
870 same mean and standard deviation as the experimental data for each visually responsive
871 single unit. For each attention condition, we computed the CRF for each random sample
872 by applying an ordinary least square fit to a hyperbolic ratio function:

873

$$874 \quad r = r_{max} \cdot \frac{c^n}{c^n + c_{50}^n} + m \quad (1)$$

875

876 where r is the neuronal response, r_{max} is the maximum attainable response, c is the
877 contrast, c_{50} is the contrast at which response is half-maximal, m is the baseline activity,
878 and n describes the steepness of the response function and represents the neuron's
879 sensitivity to contrast. This function has been shown to provide a good fit to contrast
880 response functions from visual cortices in cat and macaque monkey (Albrecht and
881 Hamilton, 1982; Williford and Maunsell, 2006). We then averaged the best-fitting CRFs

882 across random samples to generate the mean CRF for each visually responsive single
883 unit (Figure 1D).

884

885 *Analysis of Spiking Activity:*

886 For every single unit, the spiking variability was measured by the local variation (Lv),
887 which quantifies the average differences between consecutive inter-spike intervals (ISIs).

888

889
$$Lv = \frac{3}{N-2} \sum_{i=1}^{N-1} \frac{(\Delta t_i - \Delta t_{i+1})^2}{(\Delta t_i + \Delta t_{i+1})^2} \quad (2)$$

890

891 where Δt_i is a given ISI and N represents the total number of spikes within the time
892 window. The advantage of Lv over other spiking measures such as the Fano factor and
893 coefficient of variation is that it is more robust to changes in firing rate (Shinomoto et al.,
894 2003). We computed each unit's Lv using its spike train during a stimulus flash and
895 averaged across all flashes (restricted to non-target stimuli).

896 For completely Poisson processes (where neuronal firing rates are fixed and spike times
897 are random) the Lv is 1, whereas more regular activity takes values significantly lower
898 than 1, and bursty spiking takes values significantly larger than 1.

899 Of 410 single units, we included 341 neurons with enough spikes to compute Lv for
900 further clustering analysis.

901

902 *Clustering Analysis:*

903 We used the k -means clustering algorithm (Hartigan and Wong, 1979) to characterize
904 cell classes upon the space of peak-to-trough duration (PTD) and Lv . To estimate a range
905 of the number of clusters, we used a set of indices that evaluate the quality of clustering
906 (Halkidi et al., 2001; Jain and Dubes, 1988; Milligan and Cooper, 1985; Vendramin et al.,
907 2010): Rand, Mirkin, Hubert, Silhouette, Davies–Bouldin, Calinski–Harabasz, Hartigan,
908 Homogeneity and Separation indices. We ran 50 replicates of the k -means clustering for
909 different numbers of clusters, from $k = 1$ to $k = 40$. For each k , we selected the best
910 replicate according to the minimum squared Euclidean distance from all cluster elements

911 to their respective centroids. We also ran 10 identical realizations, each with a random
912 set of initial centroids to exclude the initialization issues. We evaluated validation indices
913 for each realization, and due to random initializations, most validation indices showed
914 increased variability after saturation, suggesting excessive partitions in the clustering
915 process. Based on this method, a range of 2 to 10 clusters was shown to be proper for
916 our dataset.

917 We then used a meta-clustering analysis (Ardid et al., 2015) to select the most appropriate
918 number of clusters: we ran 500 realizations of the k -means for each k and selected the
919 best replicate from 50 replicates for each realization. After 500 realizations of each k , we
920 computed the probability that pairs of neurons belonged to a same cluster. Valid clusters
921 were identified by setting a probability threshold ($p \geq 0.9$). We considered clusters with at
922 least five single units as reliable. We identified the most appropriate number of clusters
923 ($k = 5$) as the largest number of reliable cell classes that classified the most neurons in
924 the dataset (Supp. Figure 2A).

925

926 *Clustering Validation:*

927 We validated our clustering analysis in three ways. First, we applied a data-driven
928 approach based on a form of cross-validation (Fu and Perry, 2020). We organized our
929 data into a matrix with each row representing a single unit and each column representing
930 a feature for clustering. We then randomly partition the rows and columns into K and L
931 subsets, respectively. Each fold is represented by a pair (r, s) of integers, with $r \in$
932 $\{1, \dots, K\}$ and $s \in \{1, \dots, L\}$. Fold (r, s) treats the r th row subset as “test” observations,
933 and the s th column subset as “responses”. The remaining $(K - 1)$ row subsets are “train”
934 observations, and the $(L - 1)$ column subsets are “predictors”. For our dataset, we take
935 $K = 5$ and $L = 2$. We applied the same clustering procedures described above to the
936 “responses” data of “train” observations to generate the cluster labels and cluster means
937 for “train” observations. Then, we trained a linear discriminant analysis classifier with
938 equal class priors to predict those cluster labels from the “predictors” data of “train”
939 observations. The classifier was then applied to the “predictors” data of “test”
940 observations to generate their predicted cluster labels as well as predicted cluster means.

941 The cross-validation error was then computed by averaging the squared differences
942 between the “responses” of “test” observations and their predicted cluster means. Using
943 such a method, we calculated the cross-validation error for each k (from $k = 2$ to $k = 10$)
944 in the k -means clustering results (Supp. Figure 2B), and $k = 5$ showed the lowest cross-
945 validation error.

946 Second, we validated the stability of our clustering analysis by subsampling analysis
947 (Hennig, 2007). We generated 100 random subsamples containing 90% of the trials from
948 “attend in” or “attend away” or both conditions. We computed the L_v for every single unit
949 in subsamples. Random subsamples were then clustered by the k -means algorithm with
950 k from 3 to 10. The Jaccard similarities were calculated between original clusters and
951 clusters from the subsample, and the maximum was found for each original cluster. These
952 Jaccard similarities were averaged across all subsample runs. Clusters with average
953 Jaccard similarities below 0.5 were thought to be unstable. We reported the minimum
954 Jaccard similarity across original clusters for each k (Supp. Figure 2C), and all clusters
955 when $k = 5$ were stable. A cell-wise co-clustering matrix was also generated during this
956 procedure (Supp. Figure 2D), and it also supported our estimation of cluster stability.

957 Third, we used dimensionality reduction techniques to deal with the concern that cell
958 classes in our dataset may not be separable by the linear combinations of the two features
959 we used as input to perform k -means clustering. We applied both the t-distributed
960 stochastic neighbor embedding (t-SNE; Hinton and Roweis, 2003) algorithm and the
961 uniform manifold approximation and projection (UMAP; McInnes et al., 2018) algorithm
962 to our single-unit data. Within a range of both algorithms' critical parameters, we find that
963 the clusters from k -means clustering were still well separated (Supp. Figure 2G, H).

964

965 *Attentional Modulation Index and its Contrast Dependency:*

966 The attentional modulation index (AMI) of a neuron during the stimulus presentation with
967 a specific contrast c was calculated using the best-fitting contrast response functions (r)
968 from both attention conditions:

969

970
$$AMI(c) = \frac{r(c)^{IN} - r(c)^{AWAY}}{r(c)^{IN} + r(c)^{AWAY}} \quad (3)$$

971

972 The contrast dependence of the AMI was measured by the contrast dependence index
973 (CDI):

974

975
$$CDI = \frac{\overline{AMI}_{low} - \overline{AMI}_{high}}{|\overline{AMI}_{all}|} \quad (4)$$

976 where \overline{AMI}_{low} and \overline{AMI}_{high} are the average AMIs within the low-contrast range and the
977 high-contrast range, respectively. \overline{AMI}_{all} is the average AMI across all contrasts. c_{50}
978 from the best-fitting CRF during “attend away” condition delimited the range of low
979 contrast ($c < c_{50}$) and the range of high contrast ($c \geq c_{50}$). CDI measures how the AMI of
980 a neuron fluctuates with the contrast of the stimulus. A zero CDI indicates that the AMI is
981 independent of the contrast of the stimulus. More robust attentional modulation at the low-
982 contrast range leads to positive CDIs, and more potent attention effects at the high-
983 contrast range result in negative CDIs (Figure 3B). AMI and CDI were only calculated for
984 those visually responsive neurons whose laminar locations were identified ($n = 255$).

985

986 *Normalization Model Simulations:*

987 We used the normalization model of attention (Reynolds and Heeger, 2009) to explore
988 the neural mechanisms behind the variety of attentional modulation across layers (Supp.
989 Figure 4A). The normalization model posits that the resulting firing rate (R) of the
990 population of simulated neurons can be produced from a function of the stimulus drive
991 (E), the attention field (A), and the suppressive drive (S):

992

993
$$R(c; x, \theta) = \frac{A(x, \theta)E(x, \theta; c)}{S(x, \theta; c) + \sigma} \quad (5)$$

994

995 where x and θ represent the receptive field center and orientation preference of each
996 neuron in the population. c is stimulus contrast and σ is a constant that controls the
997 contrast gain of the neurons’ response. The stimulus drive is derived from the stimulus

998 and the stimulation field of the model neuron, which is its receptive field in the spatial and
999 orientational space. The attention field describes the strength of attentional modulation
1000 as a function of receptive field center and orientation preference. The attentional
1001 modulation is 1 for unattended space and is greater than 1 for a small range of locations
1002 around the attended stimulus. We computed the suppressive drive by pooling the product
1003 of the stimulus drive and the attention field over spatial positions and orientations:

1004

$$1005 \quad S(x, \theta; c) = s(x, \theta) * [A(x, \theta)E(x, \theta; c)] \quad (6)$$

1006

1007 where $s(x, \theta)$ is the suppressive field and $*$ represents convolution. The stimulus,
1008 stimulation field (excitatory receptive field), attention field, and suppressive field all had
1009 Gaussian profile in space and orientation.

1010

1011 For simulations in Figure 4A, the stimulus size was 5 and the attention field size was 30.
1012 The CDI pattern holds for a range of stimulus sizes and attention field sizes (Supp. Figure
1013 4B). The excitatory receptive field size and the suppressive field size were varied
1014 according to their ratios relative to the attention field size. For a given pair of stimulus size
1015 and attention field size, we changed the ratio of the attention field size to the excitatory
1016 receptive field size from 0.5 to 3 and the ratio of the suppressive field size to the excitatory
1017 receptive field size from 1 to 6. The orientation tuning width of the excitatory receptive
1018 field was 60° , and the suppressive field was nonspecific. A baseline activity of 0.5 was
1019 added after the normalization. For each combination of parameters, the AMIs were
1020 calculated using the model neuron responses from two attention conditions. The CDIs of
1021 AMIs were computed from the average AMIs within the low-contrast range and the high-
1022 contrast range delimited by the CRF's inflection point from the "attend away" condition.
1023 For simulations in Supp. Figure 4C, we further modified the stimulus drive of the model
1024 to have either a nonlinear or an attention-modulated contrast response function. The
1025 nonlinear function was implemented as

$$1026 \quad r(c) = \frac{c}{c + \sigma}$$

1027 where σ is 0.26, matching the average c_{50} of our data. We also applied either a
1028 multiplicative response gain (10% of increase in overall response) or a contrast gain (1%
1029 of increase in perceived contrast) to test the effects of different attention modulation of
1030 inputs on the model neurons' responses.

1031

1032 *Computational Model:*

1033 We set up a conductance-based model of N_E excitatory (E) and N_I inhibitory (I) neurons
1034 with a connection probability of 0.5 (Figure 4B). Neurons were evenly divided into 10
1035 columns or local E-I sub-networks around a ring with the following within-column synaptic
1036 weights:

1037

1038 E to E : $w_{EE} = \frac{W_{EE}}{N_E}$; I to I : $w_{II} = \frac{W_{II}}{N_I}$; E to I : $w_{IE} = \frac{W_{IE}}{N_E}$; I to E : $w_{EI} = \frac{W_{EI}}{N_I}$

1039

1040 We only modeled E to I connections and E to E connections between different columns.

1041 The synaptic weights fell off with column distance following a Gaussian profile:

1042

1043
$$w^{ij} = \frac{W}{N_E} \times \frac{1}{\sigma\sqrt{2\pi}} \exp\left(-\frac{1}{2}\left(\frac{d_{ij}}{\sigma}\right)^2\right) \quad (7)$$

1044

1045 where w^{ij} is the synaptic weight between two columns (w_{IE}^{ij} or w_{EE}^{ij}) and d_{ij} represents
1046 the distance from column j to column i . σ controls the pooling size of the postsynaptic
1047 inhibitory (σ_I) or excitatory (σ_E) neuron.

1048 We simulated models of $N_E = 800$ excitatory and $N_I = 200$ inhibitory spiking units. The
1049 spiking units were modeled as Izhikevich neurons (Izhikevich, 2003) with the following
1050 dynamics:

1051

1052
$$\frac{dv}{dt} = 0.04v^2 + 5v + 140 - u + I \quad (8)$$

1053

1054
$$\frac{du}{dt} = a(bv - a) \quad (9)$$

1055
 1056
$$\text{if } v \geq 30 \text{ mV, then } \begin{cases} v \leftarrow c \\ u \leftarrow u + d \end{cases} \quad (10)$$

1057
 1058 v represents the membrane potential of the neuron and u is a membrane recovery
 1059 variable. I is the current input to the neuron (synaptic and injected DC currents). The
 1060 parameters a , b , c , and d determine intrinsic firing patterns and were chosen as follows:

1061
 1062 Regular spiking excitatory units: $a = 0.02, b = 0.2, c = -65, d = 8$

1063
 1064 Fast spiking inhibitory units: $a = 0.1, b = 0.2, c = -65, d = 2$

1065
 1066 Presynaptic excitatory neurons generate fast (AMPA) and slow (NMDA) synaptic currents,
 1067 while presynaptic inhibitory neurons generate fast GABA currents:

1068
 1069
$$I_{syn} = \sum_i g_{AMPA}(t)(v(t) - V_{AMPA}) + \sum_j g_{NMDA}(t)(v(t) - V_{NMDA})$$

$$+ \sum_k g_{GABA}(t)(v(t) - V_{GABA}) \quad (11)$$

1070
 1071 where $V_{AMPA} = 0$, $V_{NMDA} = 0$, $V_{GABA} = -70$ are the respective reversal potentials (mV).

1072 The synaptic time course $g(t)$ was modeled as a difference between exponentials:

1073
 1074
$$g(t) = \frac{1}{\tau_d - \tau_r} \left[\exp\left(-\frac{t - \tau_l}{\tau_d}\right) - \exp\left(-\frac{t - \tau_l}{\tau_r}\right) \right] \quad (12)$$

1075
 1076 where the parameters τ_d, τ_r , and τ_l are the decay, rise, and latency time constants with
 1077 the following values (Brunel and Wang, 2003): AMPA: $\tau_d = 2$ ms, $\tau_r = 0.5$ ms, $\tau_l = 1$ ms;
 1078 NMDA: $\tau_d = 80$ ms, $\tau_r = 2$ ms, $\tau_l = 1$ ms; GABA: $\tau_d = 5$ ms, $\tau_r = 0.5$ ms, $\tau_l = 1$ ms;
 1079 The AMPA to NMDA ratio is 0.45 (Myme et al., 2003).

1080 We simulated the network with a DC step current ($I_{DC} = 4$) of duration 1.2 s. Synaptic
1081 noise was sampled from a normal distribution ($I_{syn-noise} \sim \mathcal{N}(\mu = 0, \sigma = 3)$). We pooled
1082 over spike trains of excitatory units and inhibitory units in each column separately and
1083 calculated the shuffled-corrected jittered cross-correlations from the two population spike
1084 trains binned at 1 ms within the 200 ms time window (800-1000 ms) after the initial
1085 transient response across 500 repeats of the simulation. Cross-correlations for different
1086 choices of σ_I or σ_E were reported as the average across columns (Figure 4C) (Harrison
1087 et al., 2007; Harrison and Geman, 2009).

1088

1089 *Spike Train Cross-correlations:*

1090 The population cross-correlograms in Figure 4 report shuffled-corrected jittered cross-
1091 correlations (Harrison et al., 2007; Harrison and Geman, 2009). We computed the jittered
1092 cross-correlations by resampling two spike trains within a specific time window such that
1093 for each spike in the original data, a spike is chosen at random with replacement from
1094 within the same time window across trials, thus preserving the PSTH at the resolution of
1095 the jitter window. We computed the jittered cross-correlations with 4, 8, and 16 jitter
1096 windows, and the results of 8 jitter windows were shown. Shuffled cross-correlations were
1097 calculated by cross-correlating the first population spike train with the randomly permuted
1098 second population spike train. Both types of cross-correlations were averaged across
1099 trials and were further normalized by the geometric mean of the two spike trains' firing
1100 rates and a triangular function that corrects for the amount of overlap for the different lags.
1101 The normalized shuffled cross-correlation was then subtracted from the normalized
1102 jittered cross-correlation to produce the shuffled-corrected jittered cross-correlation.

1103

1104 **AUTHOR CONTRIBUTIONS**

1105 MPJ & ASN conceptualized the project. XW analyzed the data, previously collected by
1106 ASN, and performed the computational modeling. MPJ supervised the project. XW, MPJ
1107 and ASN wrote the manuscript.

1108 **ACKNOWLEDGEMENTS**

1109 This research was supported by NIH R00 EY025026 to MPJ, NARSAD Young
1110 Investigator Grant, Ziegler Foundation Grant and Yale Orthwein Scholar Funds to
1111 ASN, and by NEI core grant for vision research P30 EY026878 to Yale University.

1112 **SUPPLEMENTARY MATERIAL**

1113 Figures S2-S4

1114

1115 **REFERENCES**

- 1116 Adesnik, H., and Naka, A. (2018). Cracking the Function of Layers in the Sensory Cortex.
1117 *Neuron* *100*, 1028-1043.
- 1118 Adesnik, H., and Scanziani, M. (2010). Lateral competition for cortical space by layer-
1119 specific horizontal circuits. *Nature* *464*, 1155-1160.
- 1120 Albrecht, D.G., and Hamilton, D.B. (1982). Striate cortex of monkey and cat: contrast
1121 response function. *J Neurophysiol* *48*, 217-237.
- 1122 Anderson, E.B., Mitchell, J.F., and Reynolds, J.H. (2011). Attentional modulation of firing
1123 rate varies with burstiness across putative pyramidal neurons in macaque visual area V4.
1124 *J Neurosci* *31*, 10983-10992.
- 1125 Anderson, J.C., and Martin, K.A. (2006). Synaptic connection from cortical area V4 to V2
1126 in macaque monkey. *J Comp Neurol* *495*, 709-721.
- 1127 Ardid, S., Vinck, M., Kaping, D., Marquez, S., Everling, S., and Womelsdorf, T. (2015).
1128 Mapping of Functionally Characterized Cell Classes onto Canonical Circuit Operations in
1129 Primate Prefrontal Cortex. *The Journal of Neuroscience* *35*, 2975.
- 1130 Avidan, G., Harel, M., Hendler, T., Ben-Bashat, D., Zohary, E., and Malach, R. (2002).
1131 Contrast sensitivity in human visual areas and its relationship to object recognition. *J*
1132 *Neurophysiol* *87*, 3102-3116.
- 1133 Bisley, J.W., and Goldberg, M.E. (2003). Neuronal activity in the lateral intraparietal area
1134 and spatial attention. *Science* *299*, 81-86.
- 1135 Bollimunta, A., Chen, Y., Schroeder, C.E., and Ding, M. (2008). Neuronal Mechanisms of
1136 Cortical Alpha Oscillations in Awake-Behaving Macaques. *The Journal of Neuroscience*
1137 *28*, 9976.
- 1138 Borra, E., Ichinohe, N., Sato, T., Tanifuji, M., and Rockland, K.S. (2010). Cortical
1139 connections to area TE in monkey: hybrid modular and distributed organization. *Cereb*
1140 *Cortex* *20*, 257-270.
- 1141 Brunel, N., and Wang, X.J. (2003). What determines the frequency of fast network
1142 oscillations with irregular neural discharges? I. Synaptic dynamics and excitation-
1143 inhibition balance. *J Neurophysiol* *90*, 415-430.
- 1144 Bruno, R.M., and Simons, D.J. (2002). Feedforward mechanisms of excitatory and
1145 inhibitory cortical receptive fields. *J Neurosci* *22*, 10966-10975.

- 1146 Callaway, E.M. (1998). Local circuits in primary visual cortex of the macaque monkey.
1147 *Annu Rev Neurosci* *21*, 47-74.
- 1148 Carandini, M. (2004). Receptive Fields and Suppressive Fields in the Early Visual System.
1149 *Cognitive Neurosciences Iii*, Third Edition *3*, 313-326.
- 1150 Carandini, M., and Heeger, D.J. (1994). Summation and division by neurons in primate
1151 visual cortex. *Science* *264*, 1333-1336.
- 1152 Carandini, M., Heeger, D.J., and Movshon, J.A. (1997). Linearity and normalization in
1153 simple cells of the macaque primary visual cortex. *J Neurosci* *17*, 8621-8644.
- 1154 Carrasco, M., Ling, S., and Read, S. (2004). Attention alters appearance. *Nat Neurosci*
1155 *7*, 308-313.
- 1156 Cohen, M.R., and Maunsell, J.H. (2009). Attention improves performance primarily by
1157 reducing interneuronal correlations. *Nat Neurosci* *12*, 1594-1600.
- 1158 Compte, A., Constantinidis, C., Tegner, J., Raghavachari, S., Chafee, M.V., Goldman-
1159 Rakic, P.S., and Wang, X.J. (2003). Temporally irregular mnemonic persistent activity in
1160 prefrontal neurons of monkeys during a delayed response task. *J Neurophysiol* *90*, 3441-
1161 3454.
- 1162 Connors, B.W., and Gutnick, M.J. (1990). Intrinsic firing patterns of diverse neocortical
1163 neurons. *Trends Neurosci* *13*, 99-104.
- 1164 Constantinidis, C., and Goldman-Rakic, P.S. (2002). Correlated discharges among
1165 putative pyramidal neurons and interneurons in the primate prefrontal cortex. *J*
1166 *Neurophysiol* *88*, 3487-3497.
- 1167 Csicsvari, J., Hirase, H., Czurko, A., Mamiya, A., and Buzsaki, G. (1999). Oscillatory
1168 coupling of hippocampal pyramidal cells and interneurons in the behaving Rat. *J Neurosci*
1169 *19*, 274-287.
- 1170 D'Souza, R.D., and Burkhalter, A. (2017). A Laminar Organization for Selective Cortico-
1171 Cortical Communication. *Front Neuroanat* *11*, 71.
- 1172 Degenetais, E., Thierry, A.M., Glowinski, J., and Gioanni, Y. (2002). Electrophysiological
1173 properties of pyramidal neurons in the rat prefrontal cortex: an in vivo intracellular
1174 recording study. *Cereb Cortex* *12*, 1-16.
- 1175 Diester, I., and Nieder, A. (2008). Complementary contributions of prefrontal neuron
1176 classes in abstract numerical categorization. *J Neurosci* *28*, 7737-7747.
- 1177 Distler, C., Boussaoud, D., Desimone, R., and Ungerleider, L.G. (1993). Cortical
1178 connections of inferior temporal area TEO in macaque monkeys. *J Comp Neurol* *334*,
1179 125-150.
- 1180 Douglas, R.J., and Martin, K.A. (1991). A functional microcircuit for cat visual cortex. *J*
1181 *Physiol* *440*, 735-769.
- 1182 Douglas, R.J., and Martin, K.A. (2004). Neuronal circuits of the neocortex. *Annu Rev*
1183 *Neurosci* *27*, 419-451.
- 1184 Felleman, D.J., and Van Essen, D.C. (1991). Distributed hierarchical processing in the
1185 primate cerebral cortex. Paper presented at: Cereb cortex (Citeseer).
- 1186 Fioravanti, M., Carlone, O., Vitale, B., Cinti, M.E., and Clare, L. (2005). A meta-analysis
1187 of cognitive deficits in adults with a diagnosis of schizophrenia. *Neuropsychol Rev* *15*, 73-
1188 95.

- 1189 Fox, S.E., and Ranck, J.B., Jr. (1981). Electrophysiological characteristics of hippocampal
1190 complex-spike cells and theta cells. *Exp Brain Res* *41*, 399-410.
- 1191 Frank, L.M., Brown, E.N., and Wilson, M.A. (2001). A comparison of the firing properties
1192 of putative excitatory and inhibitory neurons from CA1 and the entorhinal cortex. *J*
1193 *Neurophysiol* *86*, 2029-2040.
- 1194 Fu, W., and Perry, P.O. (2020). Estimating the Number of Clusters Using Cross-Validation.
1195 *Journal of Computational and Graphical Statistics* *29*, 162-173.
- 1196 Gattass, R., Galkin, T.W., Desimone, R., and Ungerleider, L.G. (2014). Subcortical
1197 connections of area V4 in the macaque. *J Comp Neurol* *522*, 1941-1965.
- 1198 Ghose, G.M., and Maunsell, J.H. (2008). Spatial summation can explain the attentional
1199 modulation of neuronal responses to multiple stimuli in area V4. *J Neurosci* *28*, 5115-
1200 5126.
- 1201 Gilbert, C.D. (1977). Laminar differences in receptive field properties of cells in cat
1202 primary visual cortex. *J Physiol* *268*, 391-421.
- 1203 Gilbert, C.D., and Wiesel, T.N. (1985). Intrinsic connectivity and receptive field properties
1204 in visual cortex. *Vision Res* *25*, 365-374.
- 1205 Gouwens, N.W., Sorensen, S.A., Berg, J., Lee, C., Jarsky, T., Ting, J., Sunkin, S.M., Feng,
1206 D., Anastassiou, C.A., Barkan, E., *et al.* (2019). Classification of electrophysiological and
1207 morphological neuron types in the mouse visual cortex. *Nat Neurosci* *22*, 1182-1195.
- 1208 Halkidi, M., Batistakis, Y., and Vazirgiannis, M. (2001). On Clustering Validation
1209 Techniques. *Journal of Intelligent Information Systems* *17*, 107-145.
- 1210 Harrison, M., Amarasingham, A., and Geman, S. (2007). Jitter methods for investigating
1211 spike train dependencies. *Computational and Systems Neuroscience Abstracts* III-17.
- 1212 Harrison, M.T., and Geman, S. (2009). A rate and history-preserving resampling algorithm
1213 for neural spike trains. *Neural Comput* *21*, 1244-1258.
- 1214 Hartigan, J.A., and Wong, M.A. (1979). Algorithm AS 136: A K-Means Clustering
1215 Algorithm. *Journal of the Royal Statistical Society Series C (Applied Statistics)* *28*, 100-
1216 108.
- 1217 Hawken, M.J., Shapley, R.M., Disney, A.A., Garcia-Marin, V., Henrie, A., Henry, C.A.,
1218 Johnson, E.N., Joshi, S., Kelly, J.G., Ringach, D.L., *et al.* (2020). Functional Clusters of
1219 Neurons in Layer 6 of Macaque V1. *J Neurosci* *40*, 2445-2457.
- 1220 Hennig, C. (2007). Cluster-wise assessment of cluster stability. *Computational Statistics*
1221 *& Data Analysis* *52*, 258-271.
- 1222 Herrmann, K., Montaser-Kouhsari, L., Carrasco, M., and Heeger, D.J. (2010). When size
1223 matters: attention affects performance by contrast or response gain. *Nat Neurosci* *13*,
1224 1554-1559.
- 1225 Hinton, G.E., and Roweis, S.T. (2003). Stochastic neighbor embedding. Paper presented
1226 at: *Advances in neural information processing systems*.
- 1227 Hirsch, J.A., and Gilbert, C.D. (1991). Synaptic physiology of horizontal connections in
1228 the cat's visual cortex. *J Neurosci* *11*, 1800-1809.
- 1229 Hirsch, J.A., and Martinez, L.M. (2006). Laminar processing in the visual cortical column.
1230 *Curr Opin Neurobiol* *16*, 377-384.
- 1231 Huang, L., and Dobkins, K.R. (2005). Attentional effects on contrast discrimination in
1232 humans: evidence for both contrast gain and response gain. *Vision Res* *45*, 1201-1212.

- 1233 Hubel, D.H., and Wiesel, T.N. (1962). Receptive fields, binocular interaction and
1234 functional architecture in the cat's visual cortex. *J Physiol* *160*, 106-154.
- 1235 Hussar, C.R., and Pasternak, T. (2009). Flexibility of sensory representations in prefrontal
1236 cortex depends on cell type. *Neuron* *64*, 730-743.
- 1237 Izhikevich, E.M. (2003). Simple model of spiking neurons. *IEEE Trans Neural Netw* *14*,
1238 1569-1572.
- 1239 Jain, A.K., and Dubes, R.C. (1988). Algorithms for clustering data (Prentice-Hall, Inc.).
- 1240 Johnston, K., DeSouza, J.F., and Everling, S. (2009). Monkey prefrontal cortical
1241 pyramidal and putative interneurons exhibit differential patterns of activity between
1242 prosaccade and antisaccade tasks. *J Neurosci* *29*, 5516-5524.
- 1243 Kastner, S., and Ungerleider, L.G. (2000). Mechanisms of visual attention in the human
1244 cortex. *Annu Rev Neurosci* *23*, 315-341.
- 1245 Kaufman, M.T., Churchland, M.M., Santhanam, G., Yu, B.M., Afshar, A., Ryu, S.I., and
1246 Shenoy, K.V. (2010). Roles of monkey premotor neuron classes in movement preparation
1247 and execution. *J Neurophysiol* *104*, 799-810.
- 1248 Kouh, M., and Poggio, T. (2008). A canonical neural circuit for cortical nonlinear
1249 operations. *Neural Comput* *20*, 1427-1451.
- 1250 Li, X., and Basso, M.A. (2008). Preparing to move increases the sensitivity of superior
1251 colliculus neurons. *J Neurosci* *28*, 4561-4577.
- 1252 Li, X., Lu, Z.L., Tjan, B.S., Doshier, B.A., and Chu, W. (2008). Blood oxygenation level-
1253 dependent contrast response functions identify mechanisms of covert attention in early
1254 visual areas. *Proc Natl Acad Sci U S A* *105*, 6202-6207.
- 1255 Martinez-Trujillo, J., and Treue, S. (2002). Attentional modulation strength in cortical area
1256 MT depends on stimulus contrast. *Neuron* *35*, 365-370.
- 1257 McAdams, C.J., and Maunsell, J.H. (1999a). Effects of attention on orientation-tuning
1258 functions of single neurons in macaque cortical area V4. *J Neurosci* *19*, 431-441.
- 1259 McAdams, C.J., and Maunsell, J.H. (1999b). Effects of attention on the reliability of
1260 individual neurons in monkey visual cortex. *Neuron* *23*, 765-773.
- 1261 McCormick, D.A., Connors, B.W., Lighthall, J.W., and Prince, D.A. (1985). Comparative
1262 electrophysiology of pyramidal and sparsely spiny stellate neurons of the neocortex. *J*
1263 *Neurophysiol* *54*, 782-806.
- 1264 McInnes, L., Healy, J., and Melville, J. (2018). Umap: Uniform manifold approximation
1265 and projection for dimension reduction. arXiv preprint arXiv:180203426.
- 1266 McIntyre, R.S., Kennedy, S.H., Soczynska, J.K., Nguyen, H.T., Bilkey, T.S.,
1267 Woldeyohannes, H.O., Nathanson, J.A., Joshi, S., Cheng, J.S., Benson, K.M., *et al.*
1268 (2010). Attention-deficit/hyperactivity disorder in adults with bipolar disorder or major
1269 depressive disorder: results from the international mood disorders collaborative project.
1270 *Prim Care Companion J Clin Psychiatry* *12*, PCC.09m00861.
- 1271 Mehta, A.D., Ulbert, I., and Schroeder, C.E. (2000). Intermodal selective attention in
1272 monkeys. II: physiological mechanisms of modulation. *Cereb Cortex* *10*, 359-370.
- 1273 Migliore, M., and Shepherd, G.M. (2005). Opinion: an integrated approach to classifying
1274 neuronal phenotypes. *Nat Rev Neurosci* *6*, 810-818.
- 1275 Milligan, G.W., and Cooper, M.C. (1985). An examination of procedures for determining
1276 the number of clusters in a data set. *Psychometrika* *50*, 159-179.

- 1277 Mitchell, J.F., Sundberg, K.A., and Reynolds, J.H. (2007). Differential attention-
1278 dependent response modulation across cell classes in macaque visual area V4. *Neuron*
1279 *55*, 131-141.
- 1280 Mitchell, J.F., Sundberg, K.A., and Reynolds, J.H. (2009). Spatial attention decorrelates
1281 intrinsic activity fluctuations in macaque area V4. *Neuron* *63*, 879-888.
- 1282 Mitzdorf, U. (1985). Current source-density method and application in cat cerebral cortex:
1283 investigation of evoked potentials and EEG phenomena. *Physiological Reviews* *65*, 37-
1284 100.
- 1285 Moore, T., and Zirnsak, M. (2017). Neural Mechanisms of Selective Visual Attention.
1286 *Annu Rev Psychol* *68*, 47-72.
- 1287 Moran, J., and Desimone, R. (1985). Selective attention gates visual processing in the
1288 extrastriate cortex. *Science* *229*, 782-784.
- 1289 Morrone, M.C., Denti, V., and Spinelli, D. (2002). Color and luminance contrasts attract
1290 independent attention. *Curr Biol* *12*, 1134-1137.
- 1291 Motter, B.C. (1993). Focal attention produces spatially selective processing in visual
1292 cortical areas V1, V2, and V4 in the presence of competing stimuli. *J Neurophysiol* *70*,
1293 909-919.
- 1294 Myme, C.I., Sugino, K., Turrigiano, G.G., and Nelson, S.B. (2003). The NMDA-to-AMPA
1295 ratio at synapses onto layer 2/3 pyramidal neurons is conserved across prefrontal and
1296 visual cortices. *J Neurophysiol* *90*, 771-779.
- 1297 Naka, A., and Adesnik, H. (2016). Inhibitory Circuits in Cortical Layer 5. *Front Neural*
1298 *Circuits* *10*, 35.
- 1299 Nandy, A., Nassi, J.J., Jadi, M.P., and Reynolds, J. (2019). Optogenetically induced low-
1300 frequency correlations impair perception. *Elife* *8*, e35123.
- 1301 Nandy, A.S., Nassi, J.J., and Reynolds, J.H. (2017). Laminar Organization of Attentional
1302 Modulation in Macaque Visual Area V4. *Neuron* *93*, 235-246.
- 1303 Neuchterlein, K.H., Dawson, M.E., Ventura, J., Miklowitz, D., and Konishi, G. (1991).
1304 Information-processing anomalies in the early course of schizophrenia and bipolar
1305 disorder. *Schizophrenia Research* *5*, 195-196.
- 1306 Nowak, L.G., Azouz, R., Sanchez-Vives, M.V., Gray, C.M., and McCormick, D.A. (2003).
1307 Electrophysiological classes of cat primary visual cortical neurons in vivo as revealed by
1308 quantitative analyses. *J Neurophysiol* *89*, 1541-1566.
- 1309 Olsen, S.R., Bortone, D.S., Adesnik, H., and Scanziani, M. (2012). Gain control by layer
1310 six in cortical circuits of vision. *Nature* *483*, 47-52.
- 1311 Ostojic, S., Brunel, N., and Hakim, V. (2009). How connectivity, background activity, and
1312 synaptic properties shape the cross-correlation between spike trains. *J Neurosci* *29*,
1313 10234-10253.
- 1314 Pestilli, F., Ling, S., and Carrasco, M. (2009). A population-coding model of attention's
1315 influence on contrast response: Estimating neural effects from psychophysical data.
1316 *Vision Res* *49*, 1144-1153.
- 1317 Petersen, S.E., and Posner, M.I. (2012). The attention system of the human brain: 20
1318 years after. *Annu Rev Neurosci* *35*, 73-89.
- 1319 Pooresmaeili, A., Poort, J., Thiele, A., and Roelfsema, P.R. (2010). Separable codes for
1320 attention and luminance contrast in the primary visual cortex. *J Neurosci* *30*, 12701-12711.

- 1321 Povysheva, N.V., Gonzalez-Burgos, G., Zaitsev, A.V., Kroner, S., Barrionuevo, G., Lewis,
1322 D.A., and Krimer, L.S. (2006). Properties of excitatory synaptic responses in fast-spiking
1323 interneurons and pyramidal cells from monkey and rat prefrontal cortex. *Cereb Cortex* *16*,
1324 541-552.
- 1325 Rao, R.P., and Ballard, D.H. (1999). Predictive coding in the visual cortex: a functional
1326 interpretation of some extra-classical receptive-field effects. *Nat Neurosci* *2*, 79-87.
- 1327 Rao, S.G., Williams, G.V., and Goldman-Rakic, P.S. (1999). Isodirectional tuning of
1328 adjacent interneurons and pyramidal cells during working memory: evidence for
1329 microcolumnar organization in PFC. *J Neurophysiol* *81*, 1903-1916.
- 1330 Reynolds, J.H., and Chelazzi, L. (2004). Attentional modulation of visual processing.
1331 *Annu Rev Neurosci* *27*, 611-647.
- 1332 Reynolds, J.H., Chelazzi, L., and Desimone, R. (1999). Competitive mechanisms
1333 subserve attention in macaque areas V2 and V4. *J Neurosci* *19*, 1736-1753.
- 1334 Reynolds, J.H., and Heeger, D.J. (2009). The normalization model of attention. *Neuron*
1335 *61*, 168-185.
- 1336 Reynolds, J.H., Pasternak, T., and Desimone, R. (2000). Attention increases sensitivity
1337 of V4 neurons. *Neuron* *26*, 703-714.
- 1338 Rockland, K.S., and Pandya, D.N. (1979). Laminar origins and terminations of cortical
1339 connections of the occipital lobe in the rhesus monkey. *Brain Res* *179*, 3-20.
- 1340 Roe, A.W., Chelazzi, L., Connor, C.E., Conway, B.R., Fujita, I., Gallant, J.L., Lu, H., and
1341 Vanduffel, W. (2012). Toward a unified theory of visual area V4. *Neuron* *74*, 12-29.
- 1342 Rolls, E.T., and Baylis, G.C. (1986). Size and contrast have only small effects on the
1343 responses to faces of neurons in the cortex of the superior temporal sulcus of the monkey.
1344 *Exp Brain Res* *65*, 38-48.
- 1345 Saalmann, Y.B., Pinsk, M.A., Wang, L., Li, X., and Kastner, S. (2012). The pulvinar
1346 regulates information transmission between cortical areas based on attention demands.
1347 *Science* *337*, 753-756.
- 1348 Schroeder, C.E., and Lakatos, P. (2009). Low-frequency neuronal oscillations as
1349 instruments of sensory selection. *Trends in Neurosciences* *32*, 9-18.
- 1350 Schroeder, C.E., Mehta, A.D., and Givre, S.J. (1998). A spatiotemporal profile of visual
1351 system activation revealed by current source density analysis in the awake macaque.
1352 *Cerebral Cortex* *8*, 575-592.
- 1353 Shinomoto, S., Kim, H., Shimokawa, T., Matsuno, N., Funahashi, S., Shima, K., Fujita, I.,
1354 Tamura, H., Doi, T., Kawano, K., *et al.* (2009). Relating neuronal firing patterns to
1355 functional differentiation of cerebral cortex. *PLoS Comput Biol* *5*, e1000433.
- 1356 Shinomoto, S., Shima, K., and Tanji, J. (2003). Differences in Spiking Patterns Among
1357 Cortical Neurons. *Neural Computation* *15*, 2823-2842.
- 1358 Simons, D.J. (1978). Response properties of vibrissa units in rat SI somatosensory
1359 neocortex. *J Neurophysiol* *41*, 798-820.
- 1360 Sur, M., Garraghty, P.E., and Bruce, C.J. (1985). Somatosensory cortex in macaque
1361 monkeys: laminar differences in receptive field size in areas 3b and 1. *Brain Res* *342*,
1362 391-395.
- 1363 Swadlow, H.A. (2003). Fast-spike interneurons and feedforward inhibition in awake
1364 sensory neocortex. *Cereb Cortex* *13*, 25-32.

1365 Tasic, B., Yao, Z., Graybiuck, L.T., Smith, K.A., Nguyen, T.N., Bertagnolli, D., Goldy, J.,
1366 Garren, E., Economo, M.N., Viswanathan, S., *et al.* (2018). Shared and distinct
1367 transcriptomic cell types across neocortical areas. *Nature* *563*, 72-78.
1368 Treue, S., and Martinez Trujillo, J.C. (1999). Feature-based attention influences motion
1369 processing gain in macaque visual cortex. *Nature* *399*, 575-579.
1370 Treue, S., and Maunsell, J.H. (1996). Attentional modulation of visual motion processing
1371 in cortical areas MT and MST. *Nature* *382*, 539-541.
1372 Troyer, T.W., Krukowski, A.E., Priebe, N.J., and Miller, K.D. (1998). Contrast-invariant
1373 orientation tuning in cat visual cortex: thalamocortical input tuning and correlation-based
1374 intracortical connectivity. *J Neurosci* *18*, 5908-5927.
1375 Ungerleider, L.G., Galkin, T.W., Desimone, R., and Gattass, R. (2008). Cortical
1376 connections of area V4 in the macaque. *Cereb Cortex* *18*, 477-499.
1377 Vaiceliunaite, A., Eriskien, S., Franzen, F., Katzner, S., and Busse, L. (2013). Spatial
1378 integration in mouse primary visual cortex. *J Neurophysiol* *110*, 964-972.
1379 Van Essen, D.C., and Maunsell, J.H.R. (1983). Hierarchical organization and functional
1380 streams in the visual cortex. *Trends in Neurosciences* *6*, 370-375.
1381 Vendramin, L., Campello, R.J.G.B., and Hruschka, E.R. (2010). Relative clustering
1382 validity criteria: A comparative overview. *Statistical Analysis and Data Mining: The ASA*
1383 *Data Science Journal* *3*, 209-235.
1384 Verghese, P. (2001). Visual search and attention: a signal detection theory approach.
1385 *Neuron* *31*, 523-535.
1386 Williford, T., and Maunsell, J.H.R. (2006). Effects of Spatial Attention on Contrast
1387 Response Functions in Macaque Area V4. *J Neurophysiol* *96*, 40-54.
1388 Wilson, F.A., O'Scalaidhe, S.P., and Goldman-Rakic, P.S. (1994). Functional synergism
1389 between putative gamma-aminobutyrate-containing neurons and pyramidal neurons in
1390 prefrontal cortex. *Proc Natl Acad Sci U S A* *91*, 4009-4013.
1391 Zeng, H., and Sanes, J.R. (2017). Neuronal cell-type classification: challenges,
1392 opportunities and the path forward. *Nat Rev Neurosci* *18*, 530-546.
1393

Figure 1 - Wang

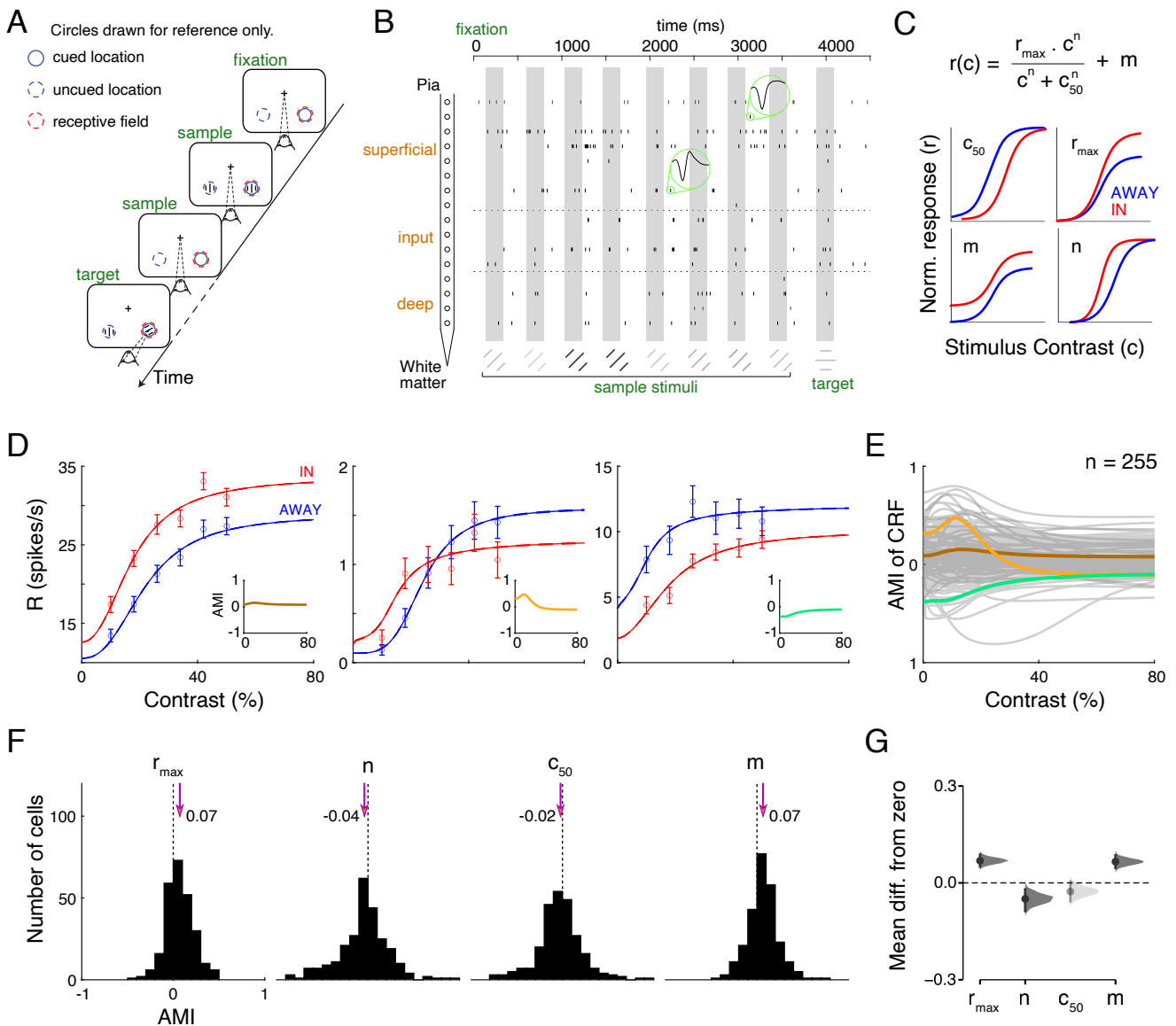


Figure 1. Attentional Modulation of Contrast Response Function

(A) Orientation change detection task. While the monkey maintained fixation, two oriented Gabor stimuli were flashed on and off at two locations: one within the RF overlap region of the recorded V4 column and the other at a location of equal eccentricity across the vertical meridian. The covert attention of the monkey was cued to one of the two locations. One of the two stimuli changed its orientation at an unpredictable time. The monkey was rewarded for making a saccade to the location of orientation change (95% probability of change at the cued location; 5% probability at uncued location [foil trials]). If no change happened (catch trials), the monkey was rewarded for maintaining fixation. Two different waveforms were shown for two single units.

(B) An example trial showing the single-unit signals in the attend-in condition. The time axis is referenced to the appearance of the fixation spot. Spikes (vertical ticks) in each channel come from the single unit with the highest spike rate in this trial. The gray boxes depict stimulus presentation epochs. In this particular trial, 8 sample stimuli with different contrasts were presented, followed by a target stimulus flash with an orientation change that the monkey responded to correctly.

(C) The mathematical function we used to fit neuronal contrast response functions is shown on the top. Schematics at the bottom show the effect of positive attentional modulation of each parameter on the contrast response function.

(D) The best-fitting contrast response functions of three example neurons in “attend in” and “attend away” conditions. Mean \pm SEM. Insets show the attentional modulation indices calculated as a function of contrast.

(E) The AMI as a function of contrast for each of the 255 visually responsive single units, with the three example units in (C) highlighted.

(F) Attention effects on the best-fitting parameters of the contrast response function. Each histogram plots the AMI distribution of a particular parameter across the population, with the dashed line marking the 0 modulation and the arrow with a number depicting the median AMI value. The median AMI is significantly different from zero for all 4 parameters (Mann-Whitney U test, $p < 0.01$).

(G) The mean difference of AMI from 0 for the 4 parameters are shown in the Cumming estimation plot. Mean differences are plotted as bootstrap sampling distributions. Each mean difference is depicted as a dot. Each 95% confidence interval (CI) is indicated by the ends of the vertical error bars. The shaded color represents that the 95% CI does not include 0.

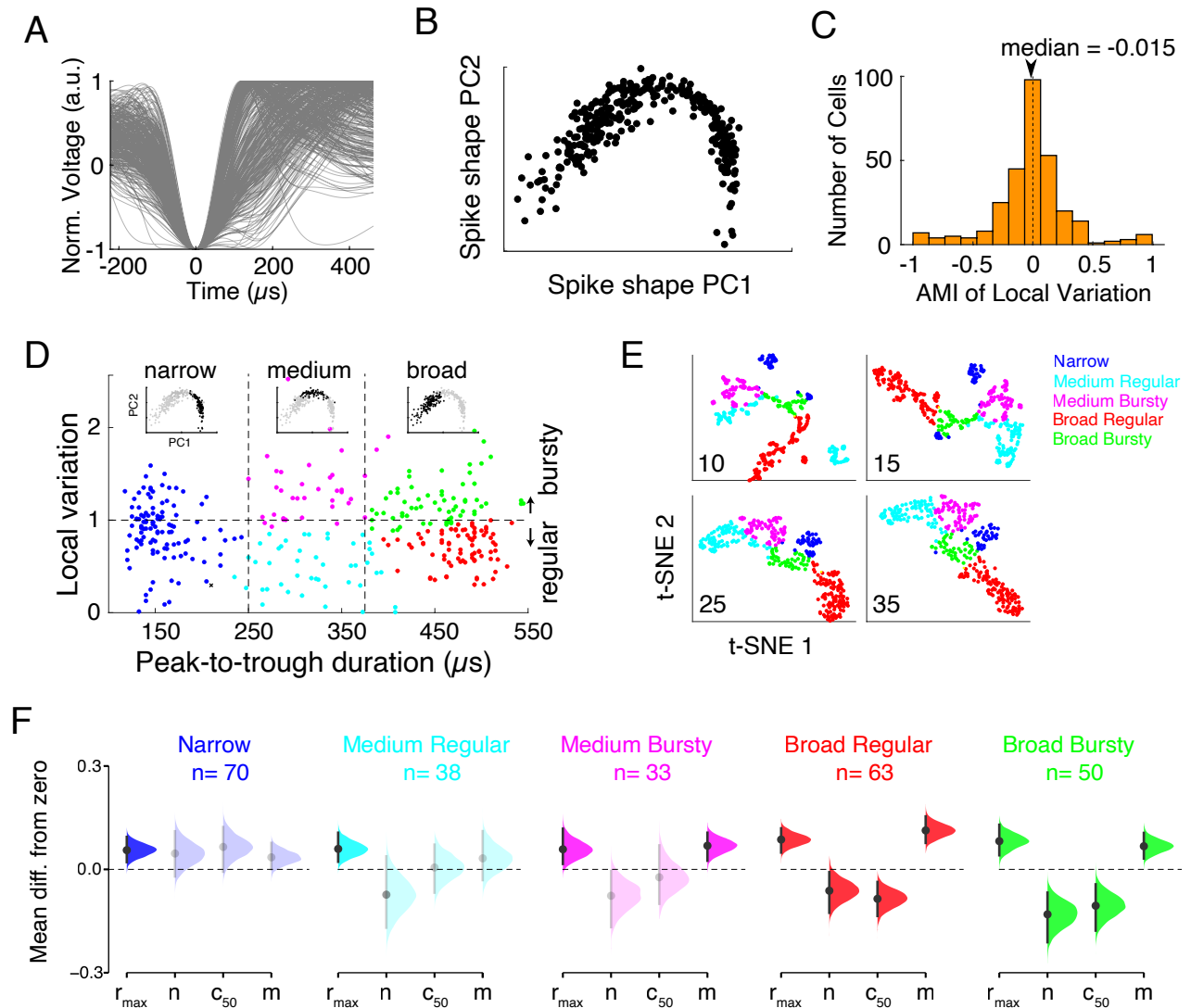


Figure 2. Classification of Single Units Using Electrophysiological Features.

(A) Mean waveforms for all 410 single units recorded. Waveform heights have been normalized to help compare spike widths.

(B) Distribution of all single units in the space of the first two principal components (PCs) of the waveforms. The non-Gaussian structure implies that spike shape is a viable feature for classifying single units.

(C) Histogram of the local variation AMI for all units with available local variation ($n=341$). The dashed line marks the 0 AMI value. The arrow depicts the median value of the distribution. The average local variation of the population is not significantly modulated by attention (Mann-Whitney U test, $p = 0.37$).

(D) k -means clustering of 341 single units based on PTD and spiking variability. Cell classes are named after their spiking widths (narrow, medium, broad) and their spiking patterns (regular, bursty). Single units within each range of spike width are highlighted in the component space on the top. Unclassified units are displayed as black crosses in the feature space.

(E) t-SNE embedding of the same data in (D) in a 2-dimensional space. The number at the left bottom corner of each panel represents the perplexity parameter of the t-SNE embedding.

(F) The Cumming estimation plot shows the bootstrap sampling distributions of AMIs of CRF parameters for each cell class. The CRF parameters were only available for visually responsive single units.

Figure 3 - Wang

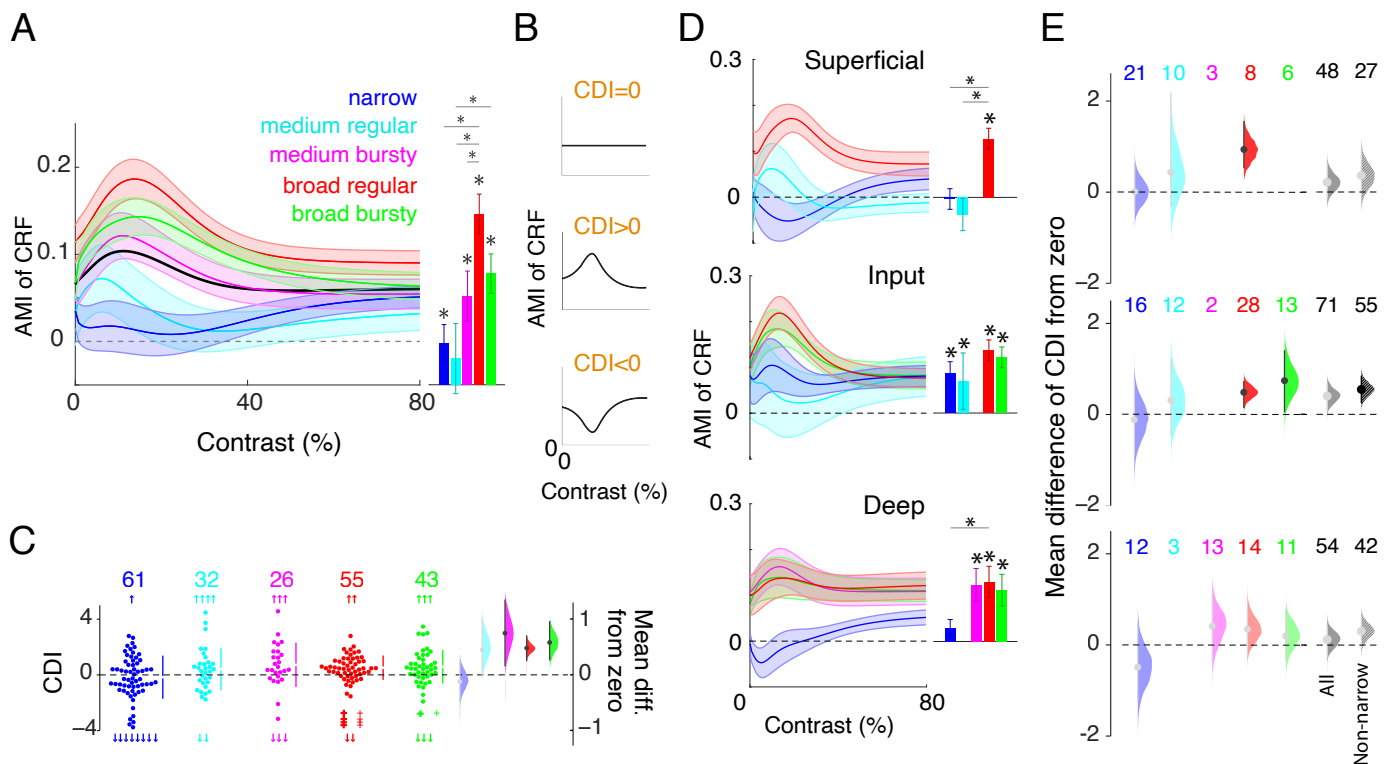


Figure 3. Contrast Dependency of AMI is Cell-Class and Layer-Specific

(A) The left panel shows the AMI of contrast responses as a function of contrast averaged across visually responsive single units in each cluster. Mean \pm SEM. The black line indicates the population mean. The right panel shows the mean AMI averaged across contrast for each cluster. Asterisk indicates either the distribution is significantly different from zero or two distributions are significantly different (Mann-Whitney U test, $p < 0.05$).

(B) To quantify the contrast dependence of attentional modulation, we averaged the AMI for a single unit separately within the low-contrast range and the high-contrast range (using the c_{50} as the low- to high-contrast threshold). We then defined the contrast dependence index (CDI) as the difference between the average AMI within the low-contrast range and that within the high-contrast range, normalized by the mean AMI across the whole contrast range. The schematic shows the interpretation of different ranges of CDI in terms of the AMI.

(C) The Cumming estimation plot shows the raw data of CDIs (left) and the bootstrap sampling distribution of the mean (right) for each cell class. The plus signs are the outliers within the axis range, and the arrows depict the outliers outside the axis limit. The number of valid units for each cell class is shown on the top of the swarm plot. Distributions for cell classes with CIs inclusive of 0 are shown in faded colors.

(D) Layer-wise AMI (mean \pm SEM) of contrast responses for each cell class as a function of contrast (left) or averaged across contrast (right). Asterisk indicates either the distribution is significantly different from zero or two distributions are significantly different (Mann-Whitney U test, $p < 0.05$). Cell classes that contain fewer than 10 units (including outliers) are excluded.

(E) Layer-wise CDI for five clusters, all units, and non-narrow units. The Cumming estimation plot shows the bootstrap sampling distribution of the mean CDI. Distributions with CIs inclusive of 0 are illustrated in faded colors. The number of units excluding outliers is shown on the top of each plot. For the raw data of the layer-wise CDIs, see Supp. Figure 3B.

Figure 4 Wang

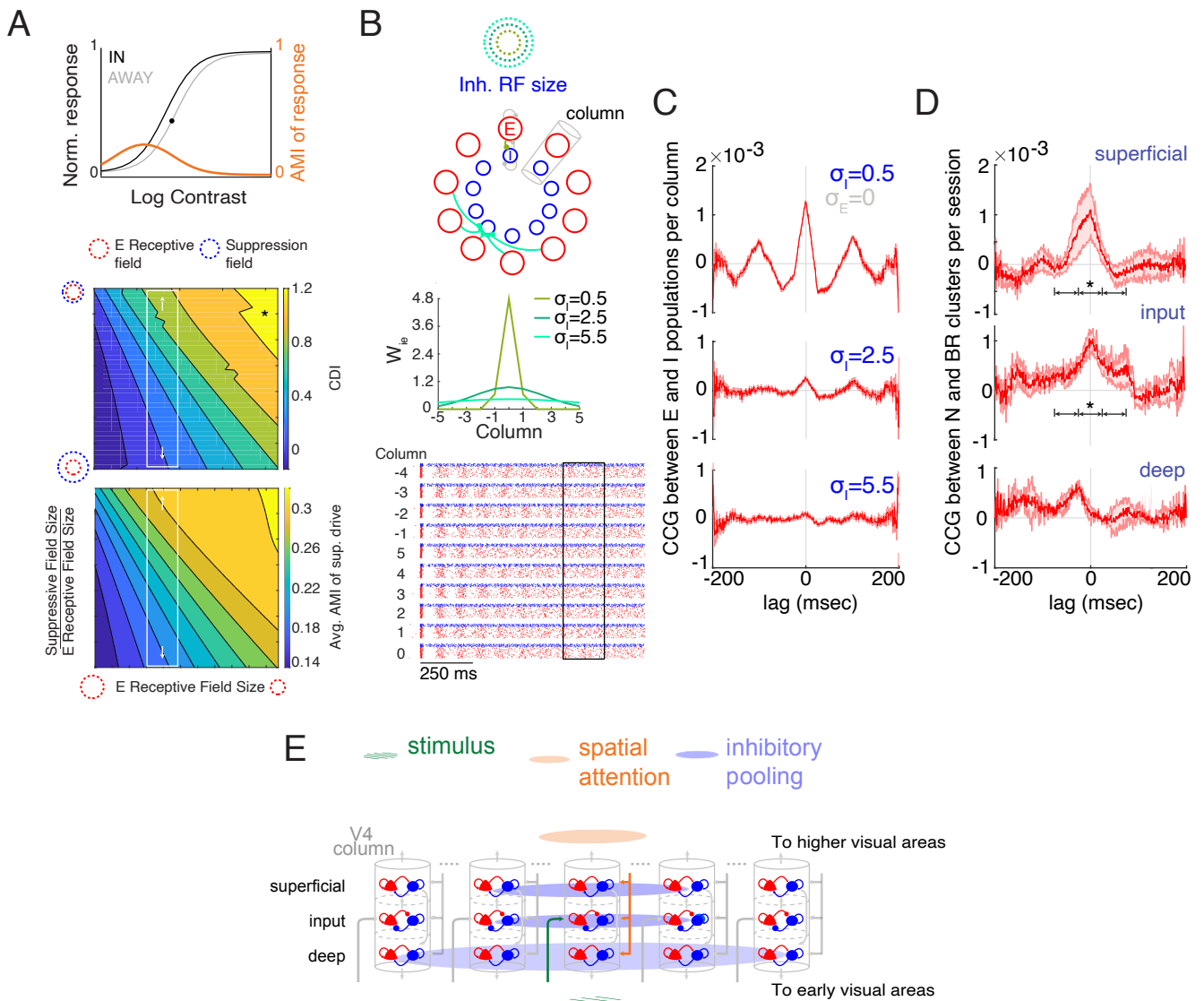


Figure 4. Computational Models Provide A Parsimonious Explanation for the Laminar Profile of AMI Contrast Dependence

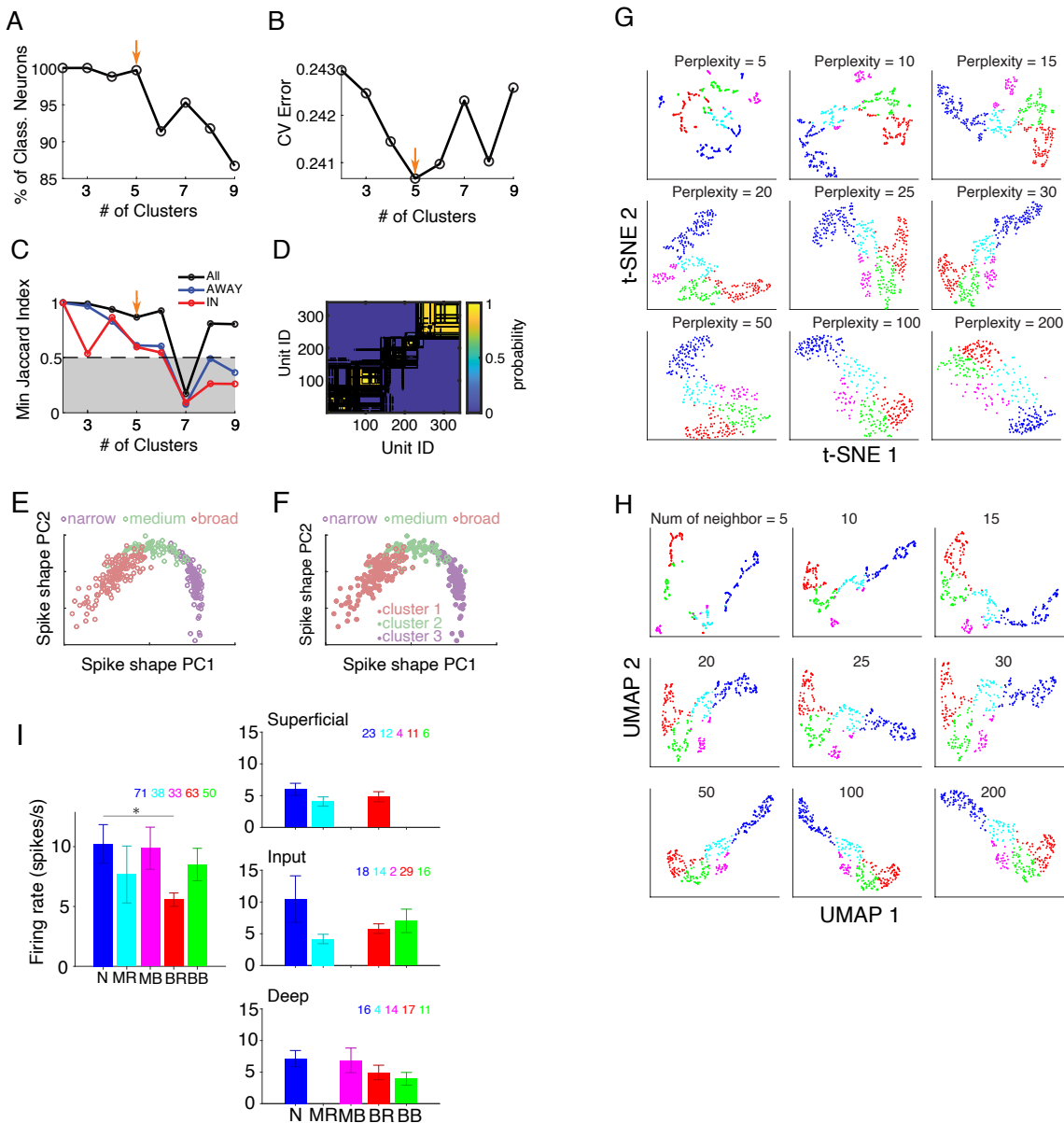
(A) Predictions from the normalization model of attention with different suppressive field sizes or different excitatory (E) receptive field sizes. The top panel shows contrast response functions for a simulated neuron in the normalization model, when attending to a stimulus within the neuron's receptive field (black curve) and when attending toward the opposite hemifield (gray curve). The orange curve represents the AMI. The black dot shows the inflection point of "attend away" responses that was used to delimit the low- and high-contrast ranges. The middle panel shows CDIs for simulated neurons as a function of the E receptive field size and the suppressive field size while holding the stimulus size and the attention field size fixed. The white rectangles depict a potential mechanism that leads to the observed variation of CDIs across layers (change in suppressive field size). The black asterisk corresponds to the model parameters used for the simulation above. The bottom panel shows AMIs of suppressive drive as a function of the E receptive field size and the suppressive field size. For both simulations, the attention field size is 30 and the stimulus size is 5. The normalization model predicts the AMI of the suppressive drive to be correlated with the CDI of neuronal responses.

(B) Simulations of a conductance-based E-I network with columnized connections. Schematics of the E-I networks corresponding to the possible mechanism in (A) are shown on top. 800 E and 200 I units were evenly distributed in 10 columns around a ring. We interpret the normalization model's suppressive field as the receptive field of inhibitory neurons in the E-I network model. E and I units from the same column are mutually coupled. We modeled I receptive field size as the standard deviations (σ_I) of E-I connections (W_{ie}) across columns (middle panel, -5 and 5 are the same column). We increased the range of E-I connections across columns (W_{ie}) (shades of green) while keeping other connections the same (gray, including W_{ee} , W_{ii} , W_{ei}). At the bottom, the raster plot shows the spiking activity for all units organized by their column IDs (blue, I; red, E) in response to a step input. The box depicts a 200 ms window used for computing cross-correlations between E and I populations.

(C) Cross-correlograms between E and I populations in the same column with different I receptive field sizes. Cross-correlations were calculated using the pooled spike trains of E units and I units from the same column across 500 repeats of identical simulation and averaged across 10 columns. A larger I receptive field reduces the cross-correlation between local E and I populations. Mean \pm SEM.

(D) Cross-correlograms (mean \pm SEM) between Narrow and Broad Regular cell classes in the superficial, input, and deep layer. Cross-correlations were calculated using the pooled spike trains of Narrow class (putative inhibitory) neurons and Broad Regular class (putative excitatory) neurons, and were averaged across sessions. The arrows mark 3 time intervals during which we averaged the cross-correlations and compared the mean differences between the superficial (or input) and the deep layers. Asterisk: The mean difference of cross-correlations in the center interval (-75 ms to 75 ms) has a 95% CI above 0. For the estimation plot, see Supp. Figure 4B.

(E) Proposed E-I networks in V4 accounting for the layer-wise CDI variations. The empirical data and the model simulations imply a larger inhibitory pooling size in the deep layer than those in the superficial and input layer. The arrows depict the canonical information flow pathways in a columnar circuit.



Supp. Figure 2. Validations for the Single-unit Classification and the AML of CRF Parameters for Each Cell Class

(A) Percentage of classified neurons in the total sample as a function of the number of clusters (k) input to the k -means clustering algorithm. The 5-cluster result was able to identify the largest set of distinct clusters while classifying most of the units.

(B) Cross-validation (CV) errors for different numbers of clusters. The 5-cluster result shows the lowest CV error.

(C) The minimum Jaccard index across clusters for each k from the subsampling analysis. The analysis was applied to neuronal data from either of the two attention conditions or to combined data. Clusters that have Jaccard indices above 0.5 are considered as stable.

(D) The cell-wise co-clustering matrix showing the probability of single units belonging to the same cluster in the subsampling analysis.

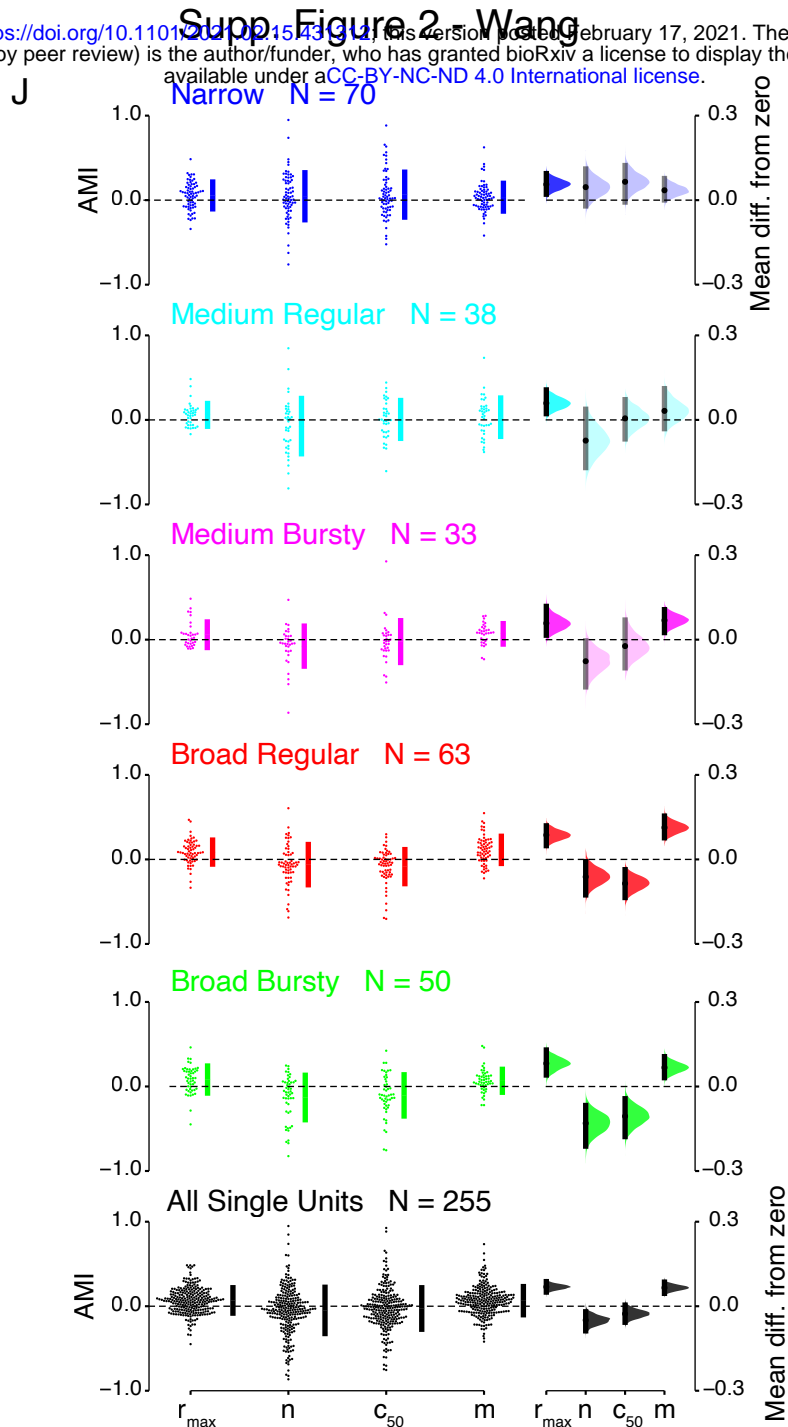
(E) In the principal component space of spike shape, we colored single units based on their spike width range (open circles; narrow, medium, broad). The clusters generated from the peak-to-trough duration were minimally overlapped.

(F) In the principal component space of spike shape, we colored single units either based on their spike width range (open circles; narrow, medium, broad) or by running the k -means clustering algorithm with the first 2 PCs (closed circles). The clusters generated from the k -means clustering match the ones grouped by the peak-to-trough duration, suggesting that peak-to-trough duration is an efficient measure to capture the variance in spike shapes.

(G and H) Embedding the data used for the k -means clustering in a 2-dimensional space using t-SNE (G) or UMAP (H).

(I) Mean firing rate for visually responsive single units split by cell class or by layer. Neuronal firing rates were calculated from stimulus flashes with the highest common contrast across two monkey experiments in the "attend away" condition. The number of single units within each cluster is shown. In each layer, we only analyzed clusters containing more than 10 single units. Asterisk indicates either the distribution is significantly different from zero or two distributions are significantly different (Mann-Whitney U test, $p < 0.05$). Mean \pm SEM.

(J) The Cumming estimation plot shows the raw data (left) of AMLs of best-fitting CRF parameters and the bootstrap sampling distribution of each cell class's mean (right).



Supp. Figure 2. Validations for the Single-unit Classification and the AMI of CRF Parameters for Each Cell Class

(A) Percentage of classified neurons in the total sample as a function of the number of clusters (k) input to the k -means clustering algorithm. The 5-cluster result was able to identify the largest set of distinct clusters while classifying most of the units.

(B) Cross-validation (CV) errors for different numbers of clusters. The 5-cluster result shows the lowest CV error.

(C) The minimum Jaccard index across clusters for each k from the subsampling analysis. The analysis was applied to neuronal data from either of the two attention conditions or to combined data. Clusters that have Jaccard indices above 0.5 are considered as stable.

(D) The cell-wise co-clustering matrix showing the probability of single units belonging to the same cluster in the subsampling analysis.

(E) In the principal component space of spike shape, we colored single units based on their spike width range (open circles; narrow, medium, broad). The clusters generated from the peak-to-trough duration were minimally overlapped.

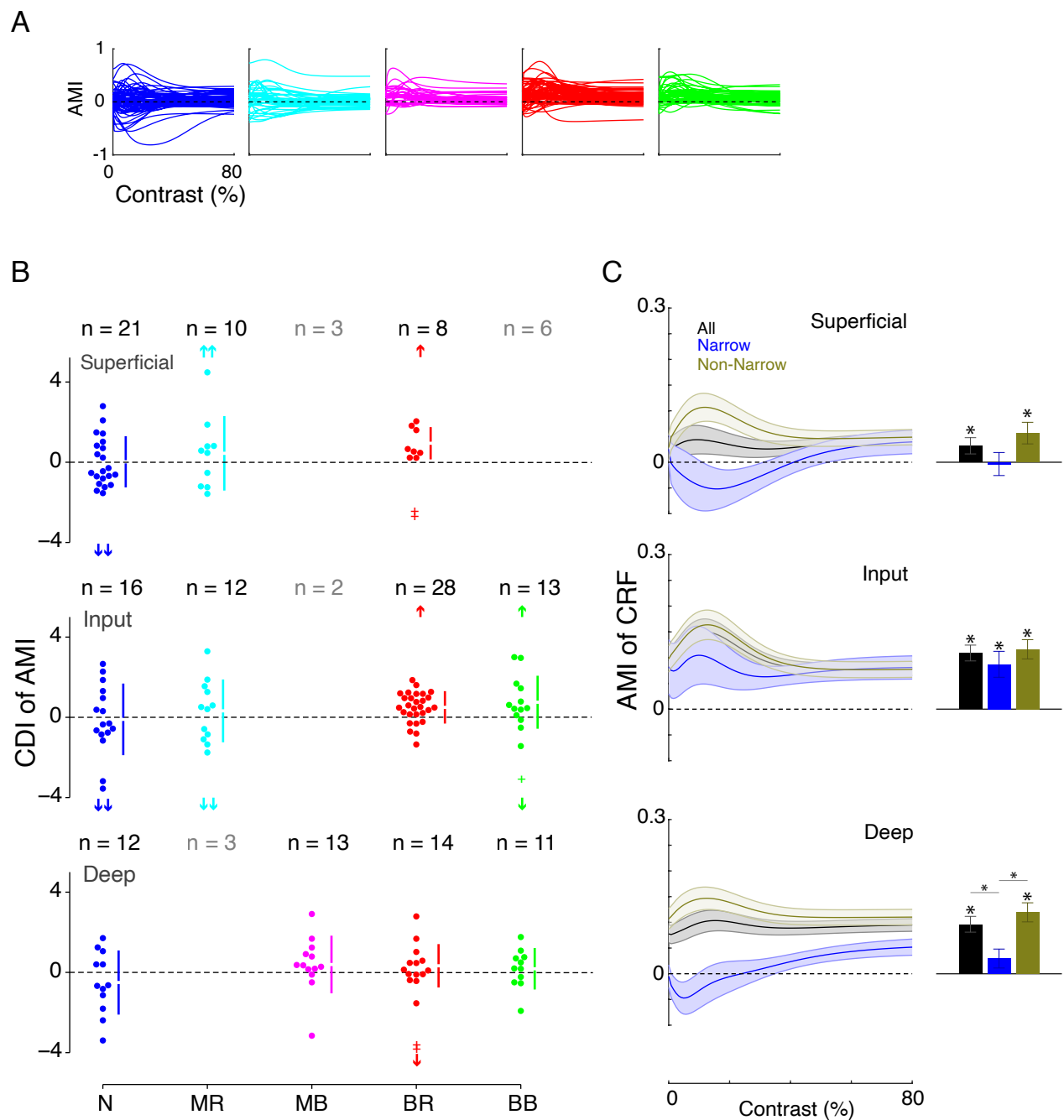
(F) In the principal component space of spike shape, we colored single units either based on their spike width range (open circles; narrow, medium, broad) or by running the k -means clustering algorithm with the first 2 PCs (closed circles). The clusters generated from the k -means clustering match the ones grouped by the peak-to-trough duration, suggesting that peak-to-trough duration is an efficient measure to capture the variance in spike shapes.

(G and H) Embedding the data used for the k -means clustering in a 2-dimensional space using t-SNE (G) or UMAP (H).

(I) Mean firing rate for visually responsive single units split by cell class or by layer. Neuronal firing rates were calculated from stimulus flashes with the highest common contrast across two monkey experiments in the "attend away" condition. The number of single units within each cluster is shown. In each layer, we only analyzed clusters containing more than 10 single units. Asterisk indicates either the distribution is significantly different from zero or two distributions are significantly different (Mann-Whitney U test, $p < 0.05$). Mean \pm SEM.

(J) The Cumming estimation plot shows the raw data (left) of AMIs of best-fitting CRF parameters and the bootstrap sampling distribution of each cell class's mean (right).

Supp. Figure 3 Wang



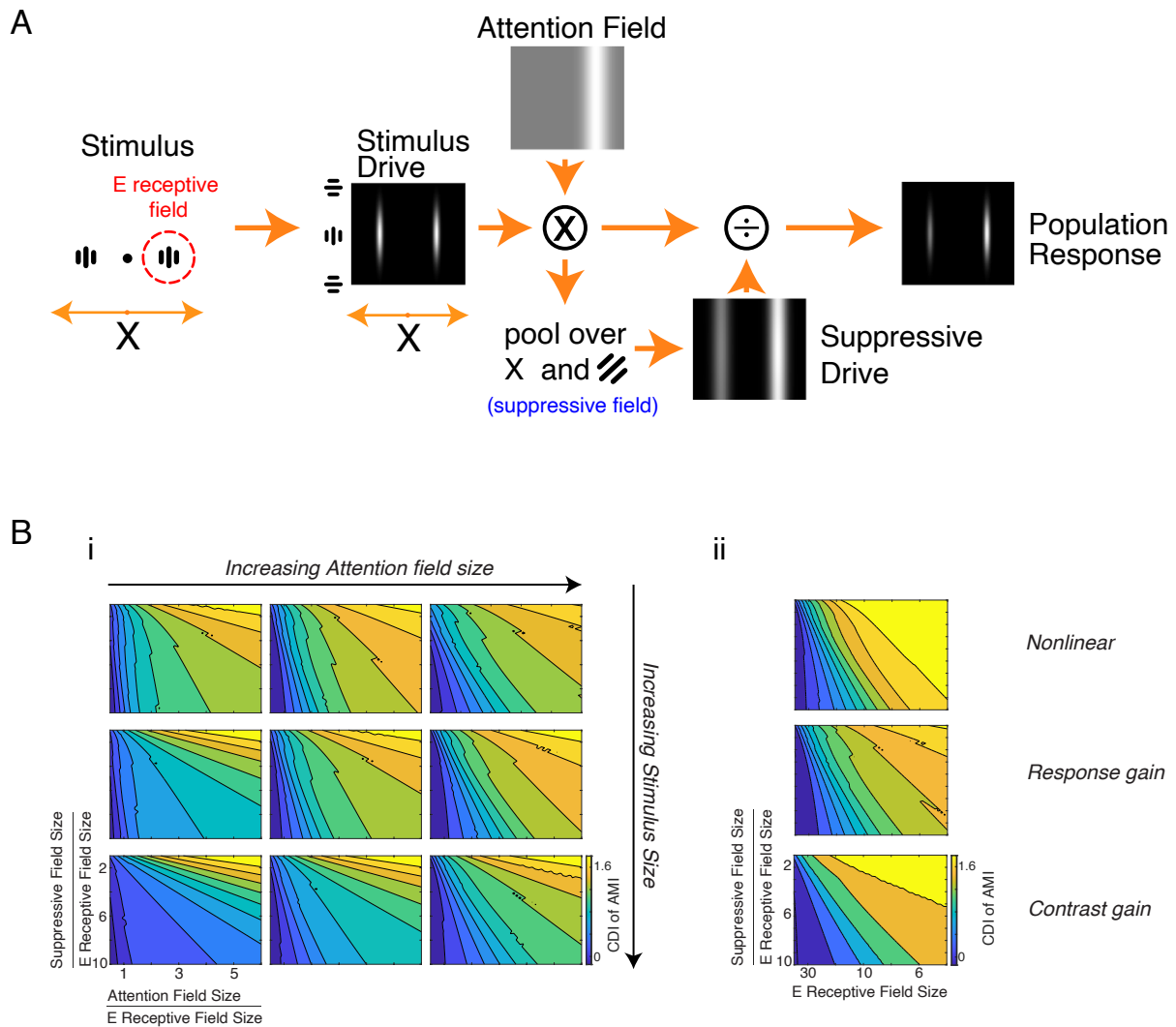
Supp. Figure 3. Raw Data of AMIs and CDIs of AMI for Each cell class

(A) The AMI of firing rate as a function of contrast for single units within each cell class.

(B) The raw data of cluster-wise CDIs of AMI within each layer. The plus signs are the outliers within the axis range, and the arrows depict the outliers outside the axis limit. The number of valid units for each cell class is shown on the top of the swarm plot.

(C) Layer-wise AMI (mean \pm SEM) for all units, Narrow unit, and non-narrow units as a function of contrast (left) or averaged across contrast (right). Asterisk indicates either the distribution is significantly different from zero or two distributions are significantly different (Mann-Whitney U test, $p < 0.05$).

Supp. Figure 4 - Wang



Supp. Figure 4. Normalization Model of Attention and CCG Analyses Between Cell Classes

(A) The structure of the normalization model of attention. The left panel shows a pair of orientated grating stimuli with identical contrasts, acting as input to the model. The central black dot indicates the fixation point. The dashed red circle indicates the receptive field of the model neuron centered on the grating stimulus. The stimulus drive shown in the middle panel is a collection of neural activity driven by the stimuli. Neurons are arranged based on their receptive field center (horizontal position) and orientation preference (vertical position). The values of the stimulus drive are shown by brightness. The top panel shows the attention field as a function of the receptive field center and the orientation preference. In this case, the attention is guided to the right stimulus position and does not vary with orientation. Gray areas indicate values of 1, and white areas indicate values greater than 1. The suppressive drive at the bottom is calculated from the point-by-point product of the stimulus drive and the attention field and then pooled over space and orientation according to the suppressive field size. The stimulus drive is multiplied by the attention field and then divided by the suppressive field to generate the output firing rates of model neurons (right panel).

(B) i, CDIs for simulated neurons in the normalization model with different stimulus sizes and attention field sizes. In each panel, we vary the E receptive field size relative to the attention field size (x-axis), and the suppressive field size relative to the E receptive field size (y-axis). The pattern of CDI holds for a range of values of stimulus size and attention field size. ii, CDIs for simulated neurons in the normalization model with different types of inputs. We changed the stimulus drive input to the normalization model to have either a nonlinear or an attention-modulated contrast response function. We tested both the response gain (10% increase in overall response) and the contrast gain (1% of increase in detected contrast) effects. For these simulations, the attention field size is 30 and the stimulus size is 5. The pattern of CDI holds for different types of inputs.

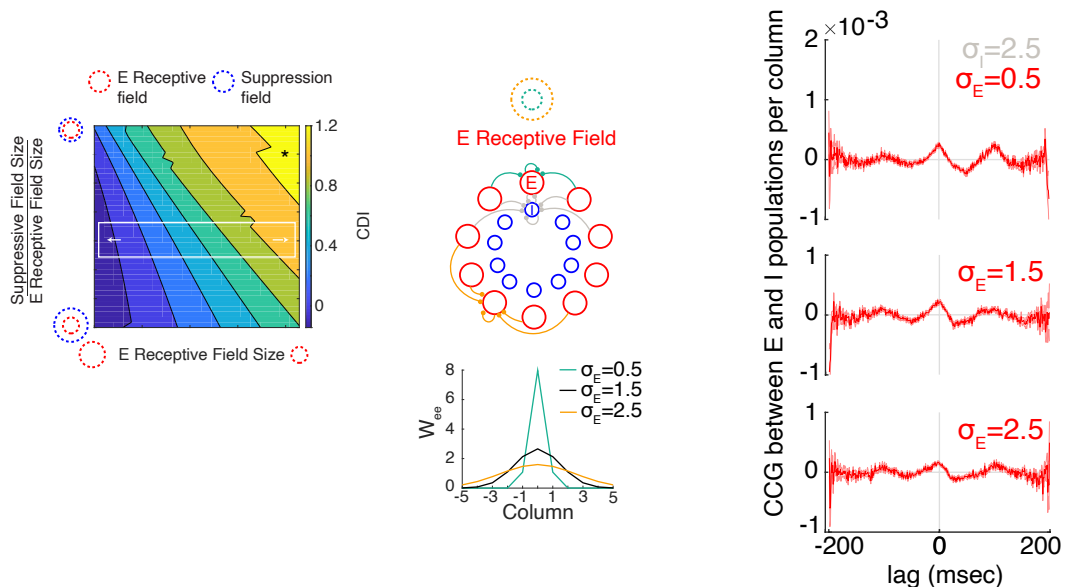
(C) Changes in E receptive field size (white box) can also lead to the variation of CDIs across layers (left panel). We tested this hypothesis in the E-I network by adjusting the standard deviation of between-column E-E connections (W_{ee}) from narrow (green) to broad (orange) while keeping other connections the same (gray, including W_{ee} , W_{ii} , W_{ie}) (middle panel). Cross-correlograms between E and I populations in the same column suggest that different E receptive field sizes have little impact on the spike-time correlations of local neural activity across layers (right panel).

(D) Cross-correlograms (mean \pm SEM) between Narrow and 3 other cell classes in the superficial, input, and deep layer. Cross-correlations were calculated using the pooled spike trains of Narrow class and the other cell class (Board Bursty, Medium Regular, or Medium Bursty) and were averaged across sessions.

(E) The Cumming estimation plot shows the mean difference for cell-class specific comparisons of average cross-correlations between the superficial (*Super.*) and deep layers or between the input and deep layers. We picked 3 time intervals to compute the average cross-correlations (rows). The raw data of average cross-correlations is plotted on the left in each panel. Each mean difference between layers is plotted on the right as a bootstrap sampling distribution.

Supp. Figure 4 - Wang

C



Supp. Figure 4. Normalization Model of Attention and CCG Analyses Between Cell Classes

(A) The structure of the normalization model of attention. The left panel shows a pair of orientated grating stimuli with identical contrasts, acting as input to the model. The central black dot indicates the fixation point. The dashed red circle indicates the receptive field of the model neuron centered on the grating stimulus. The stimulus drive shown in the middle panel is a collection of neural activity driven by the stimuli. Neurons are arranged based on their receptive field center (horizontal position) and orientation preference (vertical position). The values of the stimulus drive are shown by brightness. The top panel shows the attention field as a function of the receptive field center and the orientation preference. In this case, the attention is guided to the right stimulus position and does not vary with orientation. Gray areas indicate values of 1, and white areas indicate values greater than 1. The suppressive drive at the bottom is calculated from the point-by-point product of the stimulus drive and the attention field and then pooled over space and orientation according to the suppressive field size. The stimulus drive is multiplied by the attention field and then divided by the suppressive field to generate the output firing rates of model neurons (right panel).

(B) i, CDIs for simulated neurons in the normalization model with different stimulus sizes and attention field sizes. In each panel, we vary the E receptive field size relative to the attention field size (x-axis), and the suppressive field size relative to the E receptive field size (y-axis). The pattern of CDI holds for a range of values of stimulus size and attention field size. ii, CDIs for simulated neurons in the normalization model with different types of inputs. We changed the stimulus drive input to the normalization model to have either a nonlinear or an attention-modulated contrast response function. We tested both the response gain (10% increase in overall response) and the contrast gain (1% of increase in detected contrast) effects. For these simulations, the attention field size is 30 and the stimulus size is 5. The pattern of CDI holds for different types of inputs.

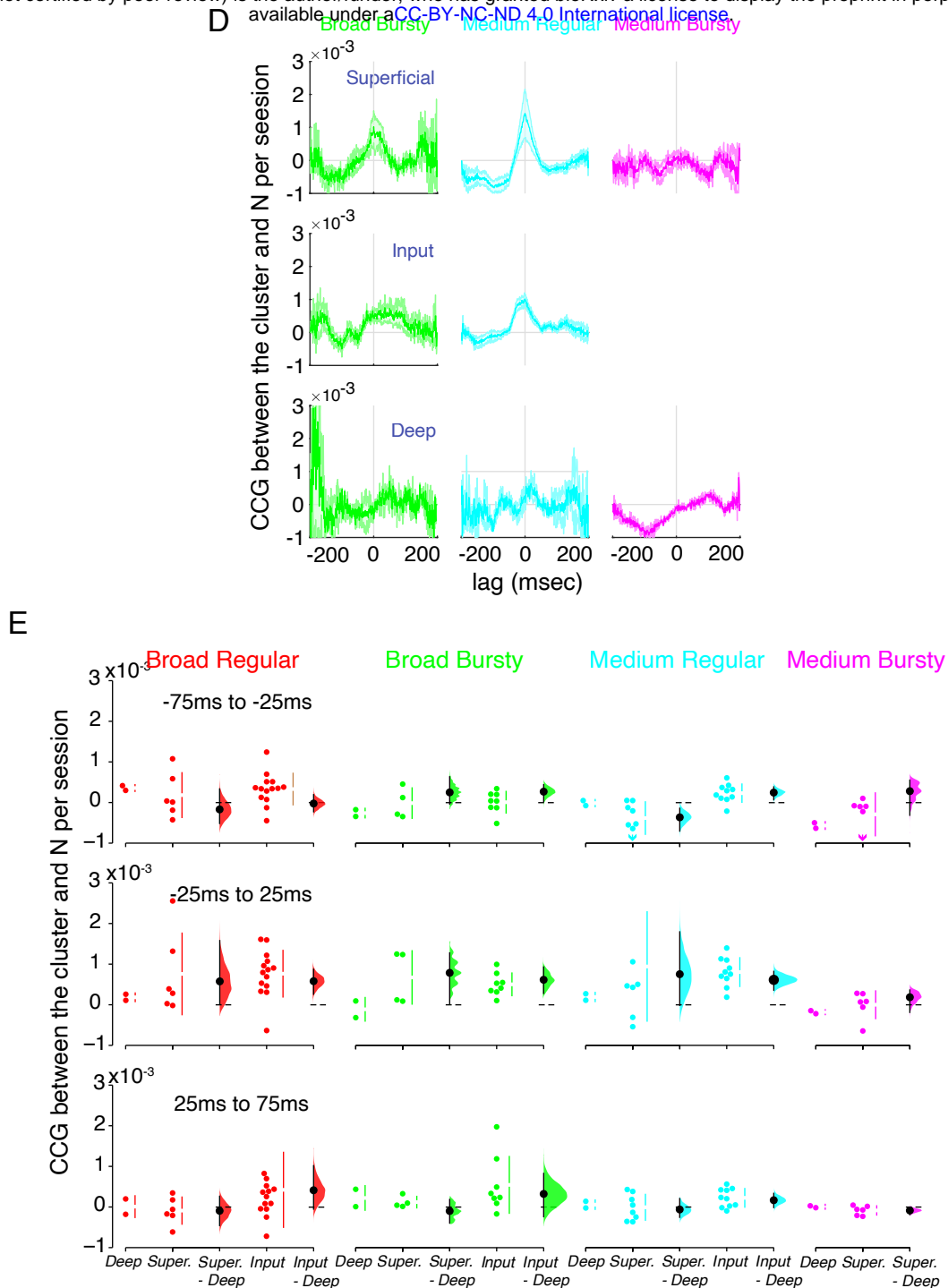
(C) Changes in E receptive field size (white box) can also lead to the variation of CDIs across layers (left panel). We tested this hypothesis in the E-I network by adjusting the standard deviation of between-column E-E connections (W_{ee}) from narrow (green) to broad (orange) while keeping other connections the same (gray, including W_{ee} , W_{ii} , W_{ie}) (middle panel). Cross-correlograms between E and I populations in the same column suggest that different E receptive field sizes have little impact on the spike-time correlations of local neural activity across layers (right panel).

(D) Cross-correlograms (mean \pm SEM) between Narrow and 3 other cell classes in the superficial, input, and deep layer. Cross-correlations were calculated using the pooled spike trains of Narrow class and the other cell class (Broad Bursty, Medium Regular, or Medium Bursty) and were averaged across sessions.

(E) The Cumming estimation plot shows the mean difference for cell-class specific comparisons of average cross-correlations between the superficial (*Super.*) and deep layers or between the input and deep layers. We picked 3 time intervals to compute the average cross-correlations (rows). The raw data of average cross-correlations is plotted on the left in each panel. Each mean difference between layers is plotted on the right as a bootstrap sampling distribution.

Supp. Figure 4 - Wang

bioRxiv preprint doi: <https://doi.org/10.1101/2021.02.15.431312>; this version posted February 17, 2021. The copyright holder for this preprint (which was not certified by peer review) is the author/funder, who has granted bioRxiv a license to display the preprint in perpetuity. It is made available under a [CC-BY-NC-ND 4.0 International license](#).



Supp. Figure 4. Normalization Model of Attention and CCG Analyses Between Cell Classes

(A) The structure of the normalization model of attention. The left panel shows a pair of orientated grating stimuli with identical contrasts, acting as input to the model. The central black dot indicates the fixation point. The dashed red circle indicates the receptive field of the model neuron centered on the grating stimulus. The stimulus drive shown in the middle panel is a collection of neural activity driven by the stimuli. Neurons are arranged based on their receptive field center (horizontal position) and orientation preference (vertical position). The values of the stimulus drive are shown by brightness. The top panel shows the attention field as a function of the receptive field center and the orientation preference. In this case, the attention is guided to the right stimulus position and does not vary with orientation. Gray areas indicate values of 1, and white areas indicate values greater than 1. The suppressive drive at the bottom is calculated from the point-by-point product of the stimulus drive and the attention field and then pooled over space and orientation according to the suppressive field size. The stimulus drive is multiplied by the attention field and then divided by the suppressive field to generate the output firing rates of model neurons (right panel).

(B) i, CDIs for simulated neurons in the normalization model with different stimulus sizes and attention field sizes. In each panel, we vary the E receptive field size relative to the attention field size (x-axis), and the suppressive field size relative to the E receptive field size (y-axis). The pattern of CDI holds for a range of values of stimulus size and attention field size. ii, CDIs for simulated neurons in the normalization model with different types of inputs. We changed the stimulus drive input to the normalization model to have either a nonlinear or an attention-modulated contrast response function. We tested both the response gain (10% increase in overall response) and the contrast gain (1% of increase in detected contrast) effects. For these simulations, the attention field size is 30 and the stimulus size is 5. The pattern of CDI holds for different types of inputs.

(C) Changes in E receptive field size (white box) can also lead to the variation of CDIs across layers (left panel). We tested this hypothesis in the E-I network by adjusting the standard deviation of between-column E-E connections (W_{ee}) from narrow (green) to broad (orange) while keeping other connections the same (gray, including W_{ee} , W_{ii} , W_{ie}) (middle panel). Cross-correlograms between E and I populations in the same column suggest that different E receptive field sizes have little impact on the spike-time correlations of local neural activity across layers (right panel).

(D) Cross-correlograms (mean \pm SEM) between Narrow and 3 other cell classes in the superficial, input, and deep layer. Cross-correlations were calculated using the pooled spike trains of Narrow class and the other cell class (Broad Bursty, Medium Regular, or Medium Bursty) and were averaged across sessions.

(E) The Cumming estimation plot shows the mean difference for cell-class specific comparisons of average cross-correlations between the superficial (*Super.*) and deep layers or between the input and deep layers. We picked 3 time intervals to compute the average cross-correlations (rows). The raw data of average cross-correlations is plotted on the left in each panel. Each mean difference between layers is plotted on the right as a bootstrap sampling distribution.